RESPACK: An ab initio tool for derivation of effective low-energy model of material

RESPACK: An *ab initio* tool for derivation of effective low-energy model of material[☆],[☆☆]

Kazuma Nakamura [a],[*], Yoshihide Yoshimoto [b], Yusuke Nomura [c], Terumasa Tadano [d], Mitsuaki Kawamura [e], Taichi Kosugi [f], Kazuyoshi Yoshimi [e], Takahiro Misawa [e], Yuichi Motoyama [e]

[a] *Quantum Physics Section, Department of Basic Sciences, Kyushu Institute of Technology, 1-1 Sensui-cho, Tobata, Kitakyushu, Fukuoka, 804-8550, Japan*
[b] *Department of Computer Science, The University of Tokyo, 7-3-1 Hongo, Bunkyo-ku, Tokyo 113-0033, Japan*
[c] *RIKEN Center for Emergent Matter Science, 2-1 Hirosawa, Wako, Saitama 351-0198, Japan*
[d] *Research Center for Magnetic and Spintronic Materials, National Institute for Materials Science, Tsukuba 305-0047, Japan*
[e] *Institute for Solid State Physics, The University of Tokyo, Kashiwa 277-8581, Japan*
[f] *Laboratory for Materials and Structures, Institute of Innovative Research, Tokyo Institute of Technology, Yokohama 226-8503, Japan*

ARTICLE INFO

ABSTRACT

RESPACK is a first-principles calculation software for evaluating the interaction parameters of materials and is able to calculate maximally localized Wannier functions, response functions based on the random phase approximation and related optical properties, and frequency-dependent electronic interaction parameters. RESPACK receives its input data from a band-calculation code using norm-conserving pseudopotentials with plane-wave basis sets. Automatic generation scripts that convert the band-structure results to the RESPACK inputs are prepared for xTAPP and Quantum ESPRESSO. An input file for specifying the RESPACK calculation conditions is designed pursuing simplicity and is given in the Fortran namelist format. RESPACK supports hybrid parallelization using OpenMP and MPI and can treat large systems including a few hundred atoms in the calculation cell.

Program summary
Program Title: RESPACK
CPC Library link to program files: https://dx.doi.org/10.17632/3cxb7474nj.1
Developer's repository link: https://sites.google.com/view/kazuma7k6r
Licensing provisions: GNU General Public Licence v3.0
Programming language: FORTRAN, PYTHON
External routines: LAPACK, BLAS, MPI
Nature of problem: Ab initio calculations for maximally localized Wannier function, response function with random-phase approximation, and matrix-element evaluations of frequency-dependent screened direct and exchange interactions. With this code, an effective low-energy model of materials is derived from first principles.
Solution method: Our method is based on *ab initio* many-body perturbation calculation and the maximally localized Wannier function calculation. The program employs the plane-wave basis set, and evaluations of matrix elements are performed with the fast Fourier transformation. The generalized tetrahedron method is used for the Brillouin Zone integral.
Additional comments including restrictions and unusual features: RESPACK supports xTAPP and Quantum ESPRESSO packages, and automatic generation scripts for converting the band-calculation results to the RESPACK inputs are prepared for these software. The current RESPACK only supports band-calculation codes using norm-conserving pseudopotentials with plane-wave basis sets. RESPACK supports hybrid parallelization using OpenMP and MPI to treat large systems in which a few hundred atoms are contained in unit cell.

---

1. Introduction

First-principles calculations based on density functional theory (DFT) [1,2] have currently been established and are widely used not only by theoretical researchers but also by experimental researchers. The users only input the crystal structure, and can easily evaluate the electronic and structural properties of materials. Density-functional calculations based on the local density approximation (LDA) are attractive due to its reasonable accuracy and low computational cost. Thanks to the recent advances in computer powers, it has successfully been applied to large-scale systems [3–8]. There are also many efforts to predict new materials by performing a huge number of DFT calculations [9,10]. On the other hand, it is well known that the LDA often fails to describe strongly-correlated electron systems [11]. Low-energy excitation and quantum fluctuations due to local interactions (on the order of several eV) dominate the low-energy properties of strongly correlated electron systems; the LDA cannot describe such quantum fluctuations. Therefore, the development of *ab initio* methods for strongly correlated materials has been an active research subject.

A well-known procedure for this attempt is the first-principle effective-model approach [11,12]. In this method, an effective model of a strongly correlated electron system is derived from first principles, and then the resulting effective model is numerically analyzed. Applying the highly accurate solvers which are able to evaluate electronic correlation accurately (exact diagonalization [13], dynamical mean field theory [14,15], many-variable variational Monte Carlo method [16–18], configuration interaction method [19], etc.) to the *ab initio* derived effective model enables quantitative understanding of real strongly correlated materials. It is important to establish a reliable *ab initio* derivation method for the effective models, and many studies have been performed for this purpose, ranging from iron-based superconductors [20–22], cuprates [23,24], nickelates [25,26], 3*d* and 4*d* transition-metal oxides [27], graphites [28], fullerides and aromatic compounds [29,30], organic compounds [31–34], zeolites [35,36], surface and interface systems [37–40], iridium oxides [41,42], lanthanides [43,44], and actinide dioxides [45,46]. In addition, handling for band-entangled system [47,48] and development of an extension scheme to a purely-low-dimensional system [49,50] have also been made. So far, development of the program was often closed at the laboratory level, and therefore, in order to spread the first-principle effective-model approach, software development and release are necessary.

In this paper, we introduce a software RESPACK [51] which contains a program group (maximally localized Wannier function and *ab initio* many body perturbation calculation) for deriving an effective low-energy model from first principles. The present paper focuses on a feature of the derivation tool for the effective model, but RESPACK has currently been extended to include the GW calculation, the spin–orbit interaction, and the electron–lattice coupling evaluation, which will be reported in the future. The present paper is organized as follows: In Section 2, we describe the methodological background. Some program details are given in Section 3. We give in Section 4 calculation procedure of RESPACK, and demonstrate in Section 5 how to install and compile of the source codes. In Section 6, we show a quantitative check for derived effective-model parameters of a cubic perovskite oxide SrVO$_3$. A summary is given in Section 7. We give in Appendix A input details for the RESPACK calculation. In Appendix B, we introduce a utility tool for transfer analysis after the RESPACK calculations.

2. Theoretical background

2.1. Effective low-energy model

We consider the derivation of the following extended Hubbard model within the two-center integrals written as

$$
\begin{aligned}
\mathcal{H} = & \sum_\sigma \sum_{\mathbf{RR}'} \sum_{ij} t_{i\mathbf{R}j\mathbf{R}'} a_{i\mathbf{R}}^{\sigma\dagger} a_{j\mathbf{R}'}^\sigma \\
& + \frac{1}{2} \sum_{\sigma\rho} \sum_{\mathbf{RR}'} \sum_{ij} \Bigg\{ U_{i\mathbf{R}j\mathbf{R}'} a_{i\mathbf{R}}^{\sigma\dagger} a_{j\mathbf{R}'}^{\rho\dagger} a_{j\mathbf{R}'}^\rho a_{i\mathbf{R}}^\sigma \\
& + J_{i\mathbf{R}j\mathbf{R}'} \big(a_{i\mathbf{R}}^{\sigma\dagger} a_{j\mathbf{R}'}^{\rho\dagger} a_{i\mathbf{R}}^\rho a_{j\mathbf{R}'}^\sigma + a_{i\mathbf{R}}^{\sigma\dagger} a_{i\mathbf{R}}^{\rho\dagger} a_{j\mathbf{R}'}^\rho a_{j\mathbf{R}'}^\sigma \big) \Bigg\},
\end{aligned}
\tag{1}
$$

where $a_{i\mathbf{R}}^{\sigma\dagger}$ and $a_{i\mathbf{R}}^\sigma$ are creation and annihilation operators, respectively, of an electron with spin σ in the ith Wannier orbital in the lattice $\mathbf{R}$. In this expression, the Wannier orbital is taken to be real. $t_{i\mathbf{R}j\mathbf{R}'}$ is a transfer integral defined as

$$
t_{i\mathbf{R}j\mathbf{R}'} = \langle \phi_{i\mathbf{R}} | \mathcal{H}_0 | \phi_{j\mathbf{R}'} \rangle = \int_V d\mathbf{r} \phi_{i\mathbf{R}}^*(\mathbf{r}) \mathcal{H}_0(\mathbf{r}) \phi_{j\mathbf{R}'}(\mathbf{r}')
\tag{2}
$$

with $|\phi_{i\mathbf{R}}\rangle = a_{i\mathbf{R}}^\dagger |0\rangle$ and the diagonal term ($i = j$, $\mathbf{R} = \mathbf{R}'$) being onsite energy. $\mathcal{H}_0$ in Eq. (2) is the one-body part of $\mathcal{H}$ and is often taken to be the Kohn–Sham (KS) Hamiltonian $\mathcal{H}_{KS}$. The integral in Eq. (2) is taken over the crystal volume V.

Effective direct-Coulomb and exchange integrals are expressed respectively as

$$
\begin{aligned}
U_{i\mathbf{R}j\mathbf{R}'}(\omega) &= \langle \phi_{i\mathbf{R}} \phi_{i\mathbf{R}} | W(\omega) | \phi_{j\mathbf{R}'} \phi_{j\mathbf{R}'} \rangle \\
&= \int_V d\mathbf{r} \int_V d\mathbf{r}' \phi_{i\mathbf{R}}^*(\mathbf{r}) \phi_{i\mathbf{R}}(\mathbf{r}) W(\mathbf{r}, \mathbf{r}', \omega) \phi_{j\mathbf{R}'}^*(\mathbf{r}') \phi_{j\mathbf{R}'}(\mathbf{r}')
\end{aligned}
\tag{3}
$$

and

$$
\begin{aligned}
J_{i\mathbf{R}j\mathbf{R}'}(\omega) &= \langle \phi_{i\mathbf{R}} \phi_{j\mathbf{R}'} | W(\omega) | \phi_{j\mathbf{R}'} \phi_{i\mathbf{R}} \rangle \\
&= \int_V d\mathbf{r} \int_V d\mathbf{r}' \phi_{i\mathbf{R}}^*(\mathbf{r}) \phi_{j\mathbf{R}'}(\mathbf{r}) W(\mathbf{r}, \mathbf{r}', \omega) \phi_{j\mathbf{R}'}^*(\mathbf{r}') \phi_{i\mathbf{R}}(\mathbf{r}')
\end{aligned}
\tag{4}
$$

with $W(\mathbf{r}, \mathbf{r}', \omega)$ being the frequency-dependent screened Coulomb interaction. In practical calculations, we evaluate $W(\mathbf{r}, \mathbf{r}', \omega)$ based on random phase approximation (RPA) with imposing the constraint to the polarization function (see Section 2.3).

The static limit of the screened direct-Coulomb $U_{i\mathbf{R}j\mathbf{R}'}(\omega)$ and exchange $J_{i\mathbf{R}j\mathbf{R}'}(\omega)$ integrals gives interaction parameters in the Hamiltonian $\mathcal{H}$, which are given by

$$
U_{i\mathbf{R}j\mathbf{R}'} = \lim_{\omega \to 0} U_{i\mathbf{R}j\mathbf{R}'}(\omega)
\tag{5}
$$

and

$$
J_{i\mathbf{R}j\mathbf{R}'} = \lim_{\omega \to 0} J_{i\mathbf{R}j\mathbf{R}'}(\omega),
\tag{6}
$$

respectively. $t_{i\mathbf{R}j\mathbf{R}'}$, $U_{i\mathbf{R}j\mathbf{R}'}(\omega)$, and $J_{i\mathbf{R}j\mathbf{R}'}(\omega)$ have the lattice translational symmetry of

$$
t_{i\mathbf{0}j\mathbf{R}'-\mathbf{R}} = t_{i\mathbf{R}j\mathbf{R}'},
\tag{7}
$$

$$
U_{i\mathbf{0}j\mathbf{R}'-\mathbf{R}}(\omega) = U_{i\mathbf{R}j\mathbf{R}'}(\omega),
\tag{8}
$$

$$
J_{i\mathbf{0}j\mathbf{R}'-\mathbf{R}}(\omega) = J_{i\mathbf{R}j\mathbf{R}'}(\omega),
\tag{9}
$$

where we used $\phi_{i\mathbf{R}}(\mathbf{r}) = \phi_{i\mathbf{0}}(\mathbf{r} - \mathbf{R})$. In this paper, we focus on an *ab initio* derivation of these parameters.

2.2. Wannier function

The calculation of the Wannier function follows the algorithm for the maximally-localized Wannier function [52,53]. We note

that RESPACK-*wannier* code implements the band-disentanglement treatment [53]; the maximally-localization treatment for the Wannier spread is performed after band disentanglement. The ith Wannier function of the lattice $\mathbf{R}$ is defined as

$$\phi_{i\mathbf{R}}(\mathbf{r}) = \frac{1}{\sqrt{N_k}} \sum_{\mathbf{k}} \sum_{\alpha=N_s^{\mathbf{k}}+1}^{N_s^{\mathbf{k}}+N_b^{\mathbf{k}}} U_{\alpha i}^{\mathbf{k}} \psi_{\alpha\mathbf{k}}(\mathbf{r}) e^{-i\mathbf{k}\cdot\mathbf{R}}, \tag{10}$$

where $\mathbf{k}$ is a wave vector in the first Brillouin zone and N_k is the total number of the Monkhorst–Pack k mesh. Also, $N_s^{\mathbf{k}} + 1$ is the starting number of the KS bands used to construct the Wannier function, and $N_b^{\mathbf{k}}$ is the total number of those bands; the Wannier function is constructed from the $N_b^{\mathbf{k}}$ KS bands [from $(N_s^{\mathbf{k}} + 1)$-th to $(N_s^{\mathbf{k}} + N_b^{\mathbf{k}})$-th bands]. $N_s^{\mathbf{k}}$ and $N_b^{\mathbf{k}}$ are automatically determined from the energy-window information. $U_{\alpha i}^{\mathbf{k}}$ is a matrix that transforms the αth Bloch wave function into the ith Wannier function. The αth Bloch wave function is defined as

$$\psi_{\alpha\mathbf{k}}(\mathbf{r}) = \frac{1}{\sqrt{N_k}} \sum_{\mathbf{G}}^{N_G^{\psi}} C_{\mathbf{G}\alpha}(\mathbf{k}) \frac{1}{\sqrt{\Omega}} e^{i(\mathbf{k}+\mathbf{G})\cdot\mathbf{r}}, \tag{11}$$

where $\mathbf{G}$ is a reciprocal lattice vector, and N_G^{ψ} is the total number of the plane waves used for the expansion of the wave function, which is determined by the cutoff energy E_{cut}^{ψ} from the inequality $\frac{1}{2}|\mathbf{k}+\mathbf{G}|^2 \leq E_{cut}^{\psi}$. Ω is the volume of the unit cell. Both the Wannier function and the Bloch function are normalized for the crystal volume $V = N_k\Omega$. $C_{\mathbf{G}\alpha}(\mathbf{k})$ is the expansion coefficient of the plane wave $e^{i(\mathbf{k}+\mathbf{G})\cdot\mathbf{r}}/\sqrt{\Omega}$. By inserting Eq. (11) into Eq. (10), the Wannier function at the home cell ($\mathbf{R} = \mathbf{0}$) is written as

$$\phi_{i\mathbf{0}}(\mathbf{r}) = \frac{1}{N_k} \sum_{\mathbf{k}} \sum_{\mathbf{G}}^{N_G^{\psi}} \tilde{C}_{\mathbf{G}i}(\mathbf{k}) \frac{1}{\sqrt{\Omega}} e^{i(\mathbf{k}+\mathbf{G})\cdot\mathbf{r}} \tag{12}$$

with

$$\tilde{C}_{\mathbf{G}i}(\mathbf{k}) = \sum_{\alpha=N_s^{\mathbf{k}}+1}^{N_s^{\mathbf{k}}+N_b^{\mathbf{k}}} C_{\mathbf{G}\alpha}(\mathbf{k}) U_{\alpha i}^{\mathbf{k}}. \tag{13}$$

Here, $\tilde{C}_{\mathbf{G}i}(\mathbf{k})$ is the expansion coefficient of the plane wave for the Wannier function. The center of the ith Wannier orbital at the lattice $\mathbf{R}$ is defined as

$$\langle\mathbf{r}\rangle_{i\mathbf{R}} = \langle\phi_{i\mathbf{R}}|\mathbf{r}|\phi_{i\mathbf{R}}\rangle = \langle\phi_{i\mathbf{0}}|\mathbf{r}|\phi_{i\mathbf{0}}\rangle + \mathbf{R}. \tag{14}$$

Similarly, the spread of the Wannier orbital is defined as

$$S_{i\mathbf{R}} = \langle r^2 \rangle_{i\mathbf{R}} - |\langle\mathbf{r}\rangle_{i\mathbf{R}}|^2 = \langle r^2 \rangle_{i\mathbf{0}} - |\langle\mathbf{r}\rangle_{i\mathbf{0}}|^2 \tag{15}$$

with $\langle r^2 \rangle_{i\mathbf{R}} = \langle\phi_{i\mathbf{R}}|r^2|\phi_{i\mathbf{R}}\rangle$.

2.3. Response function with random phase approximation

In the RPA and constrained RPA, the polarization function in the plane-wave basis is written as

$$\chi_{\mathbf{G}\mathbf{G}'}(\mathbf{q}, \omega) = \frac{2}{N_k} \sum_{\mathbf{k}}^{N_k} \sum_{\alpha}^{unocc} \sum_{\beta}^{occ} \left(1 - T_{\alpha\mathbf{k}+\mathbf{q}} T_{\beta\mathbf{k}}\right)$$

$$\times M_{\alpha\beta}^{\mathbf{G}}(\mathbf{k}+\mathbf{q}, \mathbf{k}) M_{\alpha\beta}^{\mathbf{G}'}(\mathbf{k}+\mathbf{q}, \mathbf{k})^* X_{\alpha\mathbf{k}+\mathbf{q},\beta\mathbf{k}}(\omega) \tag{16}$$

with

$$M_{\alpha\beta}^{\mathbf{G}}(\mathbf{k}+\mathbf{q}, \mathbf{k}) = \langle\psi_{\alpha\mathbf{k}+\mathbf{q}}|e^{i(\mathbf{q}+\mathbf{G})\cdot\mathbf{r}}|\psi_{\beta\mathbf{k}}\rangle \tag{17}$$

and

$$X_{\alpha\mathbf{k}+\mathbf{q},\beta\mathbf{k}}(\omega) = \frac{1}{\omega - E_{\alpha\mathbf{k}+\mathbf{q}} + E_{\beta\mathbf{k}} + i\delta} - \frac{1}{\omega + E_{\alpha\mathbf{k}+\mathbf{q}} - E_{\beta\mathbf{k}} - i\delta}. \tag{18}$$

Here, $\mathbf{q}$ is a wave vector in the first Brillouin zone, ω is frequency, and indices α and β specify the unoccupied and occupied bands, respectively. The interstate matrix $M_{\alpha\beta}^{\mathbf{G}}(\mathbf{k}+\mathbf{q}, \mathbf{k})$ is evaluated using the fast Fourier transformation technique. $E_{\alpha\mathbf{k}}$ and δ in Eq. (18) are the energy of the Bloch state and the broadening factor, respectively. The quantity $X_{\alpha\mathbf{k}+\mathbf{q},\beta\mathbf{k}}(\omega)$ is calculated with the generalized tetrahedron technique [54,55] as

$$X_{\alpha\mathbf{k}+\mathbf{q},\beta\mathbf{k}}(\omega) \sim \chi(\mathbf{k}; \alpha, \beta, \mathbf{q}, \omega, \delta, \delta_a, \delta_r), \tag{19}$$

where δ_a and δ_r in Eq. (19) are parameters to judge an energy degeneracy of $E_{\alpha\mathbf{k}+\mathbf{q}}$ and $E_{\beta\mathbf{k}}$. The tetrahedron routine returns a value of $x(\mathbf{k})$ in Eq. (19), and the $\{x(\mathbf{k})\}$ data are used for the Brillouin-zone integral. On the generalized tetrahedron method, the energies inside the tetrahedron are represented by the linear interpolation of the energies that make up the four vertices of the tetrahedron, and the integral in the tetrahedron domain is performed analytically. Based on the result of the tetrahedron integrals, we calculate $\{x(\mathbf{k})\}$. $T_{\alpha\mathbf{k}}$ in Eq. (16) is the transition probability from the Wannier states $\{|\phi_{i\mathbf{R}}\rangle\}$ to the Bloch state $|\psi_{\alpha\mathbf{k}}\rangle$, which is calculated as

$$T_{\alpha\mathbf{k}} = \sum_{i}^{N_w} U_{\alpha i}^{\mathbf{k}} U_{\alpha i}^{\mathbf{k}*}, \tag{20}$$

where N_w is the total number of the Wannier orbitals and $U_{\alpha i}^{\mathbf{k}}$ is defined in Eq. (10). The quantity $T_{\alpha\mathbf{k}}$ is introduced to calculate constrained polarization [48], and, in the usual RPA, the $T_{\alpha\mathbf{k}}$ are set to zero.

The symmetric dielectric function [56] can be written with using the polarization function as

$$\epsilon_{\mathbf{G}\mathbf{G}'}(\mathbf{q}, \omega) = \delta_{\mathbf{G}\mathbf{G}'} - \frac{4\pi}{\Omega} \frac{1}{|\mathbf{q}+\mathbf{G}|} \chi_{\mathbf{G}\mathbf{G}'}(\mathbf{q}, \omega) \frac{1}{|\mathbf{q}+\mathbf{G}'|}. \tag{21}$$

When $|\mathbf{q}+\mathbf{G}|$ and $|\mathbf{q}+\mathbf{G}'|$ are large, the contribution from the second term in the right hand side is negligible and $\epsilon_{\mathbf{G}\mathbf{G}'}(\mathbf{q}, \omega) \approx \delta_{\mathbf{G}\mathbf{G}'}$. Therefore, the matrix $\chi_{\mathbf{G}\mathbf{G}'}(\mathbf{q}, \omega)$ is restricted to $N_G^{\epsilon} \times N_G^{\epsilon}$, where N_G^{ϵ} ($< N_G^{\psi}$) is the number of the plane waves used to expand the polarization function, which is determined by the cutoff energy E_{cut}^{ϵ} as an inequality $\frac{1}{2}|\mathbf{q}+\mathbf{G}|^2 \leq E_{cut}^{\epsilon}$. Since the wavefunction is expanded by the plane wave up to E_{cut}^{ψ}, the dielectric function $\epsilon_{\mathbf{G}\mathbf{G}'}(\mathbf{q}, \omega)$ must also consider the expansion up to this cutoff energy. This is important when evaluating the matrix elements of the screened Coulomb interaction by the Wannier function [see Eqs. (32) and (38)]. Thus, for $E_{cut}^{\epsilon} < \frac{1}{2}|\mathbf{q}+\mathbf{G}|^2 < E_{cut}^{\psi}$, $\epsilon_{\mathbf{G}\mathbf{G}'}(\mathbf{q}, \omega)$ is assumed to be $\epsilon_{\mathbf{G}\mathbf{G}'}(\mathbf{q}, \omega) = \delta_{\mathbf{G}\mathbf{G}'}$.

In the calculation of $\epsilon_{\mathbf{G}\mathbf{G}'}(\mathbf{q}, \omega)$, we note on our special treatment of the head component which corresponds to the $\mathbf{G} = \mathbf{G}' = \mathbf{0}$ component in the $\mathbf{q} \to \mathbf{0}$ limit. In the usual RPA case, we calculate the following [57]

$$\lim_{\mathbf{q}\to\mathbf{0}} \epsilon_{\mathbf{00}}(\mathbf{q}, \omega) = 1 - \frac{4\pi}{\Omega} \frac{\partial^2 \chi_{\mathbf{00}}(\mathbf{q}, \omega)}{\partial q^2} - \frac{(\omega_{pl}^{\mu\nu})^2}{\omega(\omega + i\delta)}. \tag{22}$$

Here, the last term results from the intraband transition, and δ is the broadening factor introduced in Eq. (18). ω_{pl} is the bare plasma frequency calculated via the Fermi-surface integral as

$$\omega_{pl}^{\mu\nu} = \frac{1}{N_k} \sum_{\mathbf{k}}^{N_k} \sum_{\alpha} \left(1 - (T_{\alpha\mathbf{k}})^2\right) p_{\alpha\alpha\mathbf{k}}^{\mu} p_{\alpha\alpha\mathbf{k}}^{\nu} \delta(E_{\alpha\mathbf{k}} - E_F), \tag{23}$$

where E_F is the Fermi energy determined in the DFT band calculation, and $p_{\alpha\alpha\mathbf{k}}^{\nu}$ is the diagonal element of the transition-moment matrix with respect to the bands as

$$p_{\alpha\beta\mathbf{k}}^{\mu} = -i\left\langle\psi_{\alpha\mathbf{k}}\left|\frac{\partial}{\partial x_{\mu}} + [V_{NL}, x_{\mu}]\right|\psi_{\beta\mathbf{k}}\right\rangle$$

$$\sim -i\left\langle\psi_{\alpha\mathbf{k}}\left|\frac{\partial}{\partial x_{\mu}}\right|\psi_{\beta\mathbf{k}}\right\rangle \tag{24}$$

with x_μ being the Cartesian coordinate. On the above evaluation, we ignore the contribution from the non-local part of the pseudopotential, V_{NL}. We note that this neglect is not so serious in the evaluation of the effective interaction, because the effective interaction is written in terms of the sum over the q points [see Eq. (30)]; in this case, the contribution from the $\mathbf{q} = 0$ to the effective interaction becomes small relatively. On the other hand, in the optical response, the non-local pseudopotential contribution may manifest itself as a significant effect, especially for the transition metals [58]. This is because the optical properties are completely the $\mathbf{q} = 0$ quantity [see Eqs. (26), (27), (28), and (29)].

For the head-component calculation in the constrained RPA, we calculate the following

$$\lim_{\mathbf{q}\to 0} \epsilon_{\mathbf{00}}(\mathbf{q}, \omega) = 1 - \frac{4\pi}{\Omega} \frac{\partial^2 \chi_{\mathbf{00}}(\mathbf{q}, \omega)}{\partial q^2}, \tag{25}$$

which is obtained by dropping the last term in the right hand side of Eq. (22). The Wannier functions are constructed to include the low-energy bands near the Fermi level, and thus, $T_{\alpha\mathbf{k}} = 1$ is expected and the bare plasma frequency $\omega_{pl}^{\mu\nu}$ in Eq. (23) becomes zero. This is why we dropped the last term in the right hand side of Eq. (22). The second derivative of the polarization function with respect to the wavenumber q in Eqs. (22) or (25) can be calculated analytically, as has been done for insulators [56].

The optical properties such as the macroscopic dielectric function $\epsilon_M(\omega)$, the electronic energy loss spectrum (EELS) $L(\omega)$, the real part of the optical conductivity $\sigma(\omega)$, and the reflectance spectrum $R(\omega)$ are also calculated from the inverse of the matrix $\epsilon_{\mathbf{GG}'}(\mathbf{q}, \omega)$ in Eqs. (21) and (22) or (25) as

$$\epsilon_M(\omega) = \lim_{\mathbf{q}\to 0} \frac{1}{\epsilon_{\mathbf{00}}^{-1}(\mathbf{q}, \omega)}, \tag{26}$$

$$L(\omega) = -\text{Im} \lim_{\mathbf{q}\to 0} \epsilon_{\mathbf{00}}^{-1}(\mathbf{q}, \omega), \tag{27}$$

$$\text{Re}[\sigma(\omega)] = \frac{\omega}{4\pi} \text{Im} \lim_{\mathbf{q}\to 0} \frac{1}{\epsilon_{\mathbf{00}}^{-1}(\mathbf{q}, \omega)}, \tag{28}$$

and

$$R(\omega) = \left| \frac{1 - \sqrt{\lim_{\mathbf{q}\to 0} \epsilon_{\mathbf{00}}^{-1}(\mathbf{q}, \omega)}}{1 + \sqrt{\lim_{\mathbf{q}\to 0} \epsilon_{\mathbf{00}}^{-1}(\mathbf{q}, \omega)}} \right|, \tag{29}$$

respectively.

2.4. Direct-Coulomb and exchange integrals

The evaluations of the interaction integrals $U_{i0jR'}(\omega)$ in Eq. (8) and $J_{i0jR'}(\omega)$ in Eq. (9) proceed as follows: First, the screened Coulomb interaction is written in the reciprocal space by using the Fourier transform as

$$W(\mathbf{r}, \mathbf{r}', \omega) = \frac{1}{N_q} \sum_{\mathbf{q}}^{N_q} \sum_{\mathbf{G}, \mathbf{G}'}^{N_G^\psi} e^{i(\mathbf{q}+\mathbf{G})\cdot\mathbf{r}} W_{\mathbf{GG}'}(\mathbf{q}, \omega) e^{-i(\mathbf{q}+\mathbf{G}')\cdot\mathbf{r}'}. \tag{30}$$

Note that the q-grid is the same as the k-grid; thus, $N_q = N_k$. $W_{\mathbf{GG}'}(\mathbf{q}, \omega)$ in the right-hand side is written with using the inverse dielectric matrix as follows:

$$W_{\mathbf{GG}'}(\mathbf{q}, \omega) = \begin{cases} \frac{4\pi}{\Omega} \frac{\epsilon_{\mathbf{GG}'}^{-1}(\mathbf{q},\omega)}{|\mathbf{q}+\mathbf{G}||\mathbf{q}+\mathbf{G}'|}, & \frac{1}{2}|\mathbf{q}+\mathbf{G}|^2 < E_{cut}^\epsilon, \\ \frac{4\pi}{\Omega} \frac{1}{|\mathbf{q}+\mathbf{G}|^2}, & E_{cut}^\epsilon < \frac{1}{2}|\mathbf{q}+\mathbf{G}|^2 < E_{cut}^\psi. \end{cases} \tag{31}$$

Note that the inverse dielectric matrix has off-diagonal elements in the first $N_G^\epsilon \times N_G^\epsilon$ block and becomes diagonal matrix with unity in the area beyond this block. By inserting Eqs. (30) and (31) into

Eq. (3) and noting the lattice-translational symmetry [Eqs. (8) and (9)], we obtain the form of

$$U_{i0jR}(\omega) = \frac{4\pi}{\Omega N_q} \sum_{\mathbf{q}}^{N_q} \sum_{\mathbf{G},\mathbf{G}'}^{N_G^\epsilon} e^{-i\mathbf{q}\cdot\mathbf{R}} \rho_{i\mathbf{q}}(\mathbf{G}) \epsilon_{\mathbf{GG}'}^{-1}(\mathbf{q}, \omega) \rho_{j\mathbf{q}}^*(\mathbf{G}')$$

$$+ \frac{4\pi}{\Omega N_q} \sum_{\mathbf{q}}^{N_q} \sum_{\mathbf{G}}^{(N_G^\epsilon+1:N_G^\psi)} e^{-i\mathbf{q}\cdot\mathbf{R}} \rho_{i\mathbf{q}}(\mathbf{G}) \rho_{j\mathbf{q}}^*(\mathbf{G}) \tag{32}$$

with

$$\rho_{i\mathbf{q}}(\mathbf{G}) = \frac{1}{|\mathbf{q}+\mathbf{G}|N_k} \sum_{\mathbf{k}}^{N_k} \langle \tilde{\phi}_{i\mathbf{k}+\mathbf{q}} | e^{i(\mathbf{q}+\mathbf{G})\cdot\mathbf{r}} | \tilde{\phi}_{j\mathbf{k}} \rangle \tag{33}$$

and $|\tilde{\phi}_{i\mathbf{k}}\rangle = \sum_{\mathbf{R}}^{N_R} |\phi_{i\mathbf{R}}\rangle e^{i\mathbf{k}\cdot\mathbf{R}}$ with N_R being the total number of the lattices in the system. The divergence of Eq. (33) in $\mathbf{q} \to \mathbf{0}$ with $\mathbf{G}=\mathbf{G}'=\mathbf{0}$ is removed by following the prescription of Ref. [59].

The dependence of the static ($\omega = 0$) direct-Coulomb integral on the distance between the two Wannier functions is evaluated via

$$U(r_{ij\mathbf{R}}) = U_{i0jR}(0), \tag{34}$$

where $r_{ij\mathbf{R}}$ is the distance between the two Wannier centers,

$$r_{ij\mathbf{R}} = \left| \langle \mathbf{r} \rangle_{j\mathbf{R}} - \langle \mathbf{r} \rangle_{i0} \right| = \left| \mathbf{R} + \langle \mathbf{r} \rangle_{j0} - \langle \mathbf{r} \rangle_{i0} \right|. \tag{35}$$

Matrix elements of the bare (or unscreened) Coulomb interaction, $U_{i0jR}^{\text{bare}} = \langle \phi_{i0}\phi_{i0} | v | \phi_{j\mathbf{R}}\phi_{j\mathbf{R}} \rangle$, are calculated with replacing $\epsilon_{\mathbf{GG}'}^{-1}(\mathbf{q}, \omega)$ of Eq. (32) by $\delta_{\mathbf{GG}'}$ as

$$U_{i0jR}^{\text{bare}} = \frac{4\pi}{\Omega N_q} \sum_{\mathbf{q}}^{N_q} \sum_{\mathbf{G}}^{N_G^\psi} e^{-i\mathbf{q}\cdot\mathbf{R}} \rho_{i\mathbf{q}}(\mathbf{G}) \rho_{j\mathbf{q}}^*(\mathbf{G}). \tag{36}$$

The dependence of U_{i0jR}^{bare} on the distance between two Wannier functions is obtained from

$$U^{\text{bare}}(r_{ij\mathbf{R}}) = U_{i0jR}^{\text{bare}}. \tag{37}$$

The parallel argument can be applied to the derivation of the screened exchange integrals in Eq. (9). The result is

$$J_{i0jR}(\omega) = \frac{4\pi}{\Omega N_q} \sum_{\mathbf{q}}^{N_q} \sum_{\mathbf{G},\mathbf{G}'}^{N_G^\epsilon} \rho_{ij\mathbf{R}\mathbf{q}}(\mathbf{G}) \epsilon_{\mathbf{GG}'}^{-1}(\mathbf{q}, \omega) \rho_{ij\mathbf{R}\mathbf{q}}^*(\mathbf{G}')$$

$$+ \frac{4\pi}{\Omega N_q} \sum_{\mathbf{q}}^{N_q} \sum_{\mathbf{G}}^{(N_G^\epsilon+1:N_G^\psi)} \rho_{ij\mathbf{R}\mathbf{q}}(\mathbf{G}) \rho_{ij\mathbf{R}\mathbf{q}}^*(\mathbf{G}) \tag{38}$$

with

$$\rho_{ij\mathbf{R}\mathbf{q}}(\mathbf{G}) = \frac{1}{N_k|\mathbf{q}+\mathbf{G}|} \sum_{\mathbf{k}}^{N_k} e^{-i\mathbf{k}\cdot\mathbf{R}} \langle \tilde{\phi}_{i\mathbf{k}+\mathbf{q}} | e^{i(\mathbf{q}+\mathbf{G})\cdot\mathbf{r}} | \tilde{\phi}_{j\mathbf{k}} \rangle. \tag{39}$$

The bare exchange integral $J_{i0jR}^{\text{bare}} = \langle \phi_{i0}\phi_{j0} | v | \phi_{j\mathbf{R}}\phi_{i\mathbf{R}} \rangle$ is given as

$$J_{i0jR}^{\text{bare}} = \frac{4\pi}{\Omega N_q} \sum_{\mathbf{q}}^{N_q} \sum_{\mathbf{G}}^{N_G^\epsilon} \rho_{ij\mathbf{R}\mathbf{q}}(\mathbf{G}) \rho_{ij\mathbf{R}\mathbf{q}}^*(\mathbf{G}). \tag{40}$$

3. Some technical aspects

3.1. Symmetry

RESPACK makes use of the space group symmetries of an input crystal structure and requires irreducible data obtained from a

band calculation. The Bloch function at a reducible k point, $\mathbf{k}$, is calculated from its irreducible part via

$$\psi_{\alpha\mathbf{k}}(\mathbf{r}) = \hat{T}\hat{R}\psi_{\alpha\mathbf{k}^*}(\mathbf{r}) = \psi_{\alpha\mathbf{k}^*}(\mathbf{R}^{-1}(\mathbf{r} - \mathbf{T})), \qquad (41)$$

where $\mathbf{k}^*$ is the corresponding irreducible k point. $\hat{R}$ and $\hat{T}$ are the operators of a rotation and a fractional translation, respectively, which are represented by the 3×3 matrix $\mathbf{R}$ and three-dimensional vector $\mathbf{T}$. Eqs. (11) and (41) leads to

$$
\begin{aligned}
\psi_{\alpha\mathbf{k}}(\mathbf{r}) &= \frac{1}{\sqrt{N_k}} \sum_{\mathbf{G}^*}^{N_G^\psi} C_{\mathbf{G}^*\alpha}(\mathbf{k}^*) \frac{1}{\sqrt{\Omega}} e^{i(\mathbf{k}^*+\mathbf{G}^*)\cdot(\mathbf{R}^{-1}(\mathbf{r}-\mathbf{T}))} \\
&= \frac{A_{pf}}{\sqrt{N_k}} \sum_{\mathbf{G}^*}^{N_G^\psi} C_{\mathbf{G}^*\alpha}(\mathbf{k}^*) e^{-i(\mathbf{R}^{-1})^t\mathbf{G}^*\cdot\mathbf{T}} \frac{e^{i(\mathbf{R}^{-1})^t(\mathbf{k}^*+\mathbf{G}^*)\cdot\mathbf{r}}}{\sqrt{\Omega}}
\end{aligned} \qquad (42)
$$

with $\mathbf{G}^*$ being reciprocal lattice vector for expansion of the wave function at the irreducible k point. The global phase factor $A_{pf} = e^{-i(\mathbf{R}^{-1})^t\mathbf{k}^*\cdot\mathbf{T}}$ is ignored in the calculation because it does not affect the results. By comparing Eq. (42) with Eq. (11), we find the following relations:

$$\mathbf{k} = (\mathbf{R}^{-1})^t\mathbf{k}^* + \boldsymbol{\Delta}_{rw}, \qquad (43)$$

$$\mathbf{G} = (\mathbf{R}^{-1})^t\mathbf{G}^* - \boldsymbol{\Delta}_{rw}, \qquad (44)$$

$$C_{\mathbf{G}\alpha}(\mathbf{k}) = C_{\mathbf{G}^*\alpha}(\mathbf{k}^*)e^{-i(\mathbf{R}^{-1})^t\mathbf{G}^*\cdot\mathbf{T}}. \qquad (45)$$

Here, $\boldsymbol{\Delta}_{rw}$ is a rewind vector which is introduced to pull back the rotated $\mathbf{k}^*$ vector to the first Brillouin zone. From Eq. (44), $\mathbf{G}^*$ and $\mathbf{G}$ have the following relationship

$$\mathbf{G}^* = \mathbf{R}^t(\mathbf{G} + \boldsymbol{\Delta}_{rw}), \qquad (46)$$

and with Eqs. (45) and (46), we obtain

$$C_{\mathbf{G}\alpha}(\mathbf{k}) = C_{\mathbf{R}^t(\mathbf{G}+\boldsymbol{\Delta}_{rw})\alpha}(\mathbf{k}^*)e^{-i(\mathbf{G}+\boldsymbol{\Delta}_{rw})\cdot\mathbf{T}}. \qquad (47)$$

More specifically, in the code, we treat $\mathbf{S} = (\mathbf{R}^{-1})^t$ instead of $\mathbf{R}$, so the following expression is practically implemented

$$C_{\mathbf{G}\alpha}(\mathbf{k}) = C_{\mathbf{S}^{-1}(\mathbf{G}+\boldsymbol{\Delta}_{rw})\alpha}(\mathbf{k}^*)e^{-i(\mathbf{G}+\boldsymbol{\Delta}_{rw})\cdot\mathbf{T}}. \qquad (48)$$

Similarly, the inverse dielectric matrix at a reducible q point is generated from the irreducible one as follows:

$$\epsilon_{\mathbf{G},\mathbf{G}'}^{-1}(\mathbf{q},\omega) = \epsilon_{\mathbf{S}^{-1}(\mathbf{G}+\boldsymbol{\Delta}_{rw}),\mathbf{S}^{-1}(\mathbf{G}'+\boldsymbol{\Delta}'_{rw})}^{-1}(\mathbf{q}^*,\omega)e^{-i(\mathbf{G}-\mathbf{G}')\cdot\mathbf{T}}. \qquad (49)$$

3.2. Frequency grid

The frequency grid of the polarization function is generated as a logarithmic grid:

$$
\omega_i = \begin{cases}
\dfrac{\Delta\omega}{s-1}\left(\exp\big[(i-1)\ln s\big] - 1\right), & i = 1, \ldots, N_{max}, \\[2ex]
E_{max}\exp\left[\ln 3 \dfrac{i-N_{max}}{N_\omega - N_{max}}\right], & i = N_{max}+, \ldots, N_\Omega.
\end{cases} \qquad (50)
$$

Here, ω_i is the ith frequency, $E_{max} = \max(\{E_{\alpha\mathbf{k}}\}) - \min(\{E_{\alpha\mathbf{k}}\})$, N_Ω is the total number of the frequency grids, and N_{max} is the total number of the frequency grids in the frequency range $0 \leq \omega_i \leq E_{max}$. By default, N_Ω and N_{max} are set to 70 and $(9N_\Omega)/10$. The parameter s in Eq. (50) is determined by solving the equation $s^{N_{max}-1} + \frac{E_{max}}{\Delta\omega}(s-1) = 1$. The resulting grids satisfy the following boundary conditions: (i) $\omega_1 = 0$, (ii) $\omega_2 = \Delta\omega$ with $\Delta\omega$ being
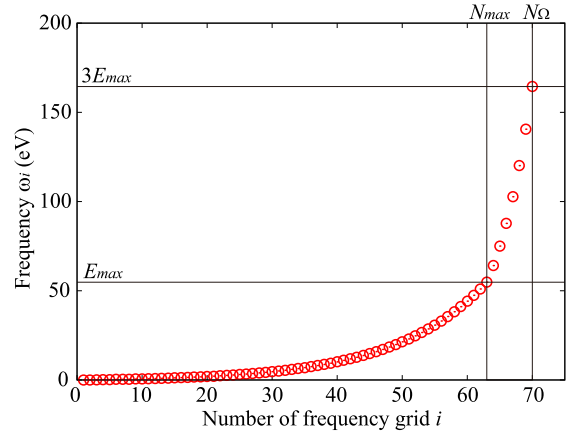
Fig. 1. Frequency grid generated with Eq. (50). This frequency grid is used to calculate the polarization function of SrVO$_3$ employed as a benchmark of this paper. In the calculation considering 50 bands (the total number of occupied bands is 15, and that of unoccupied bands is 35), E_{max} is estimated as 54.8 eV. For the calculation condition, see Section 6.1.

0.05 eV by default, (iii) $\omega_{N_{max}} = E_{max}$, and (iv) $\omega_{N_\Omega} = 3E_{max}$. An example of the generated grid is shown in Fig. 1.

3.3. Interpolation treatment

Using the resulting transfer data $t_{i0j\mathbf{R}}$ in Section 2.2, the one-body Hamiltonian matrix at an arbitrary k-point $\mathbf{k}'$ is calculated as

$$H_{ij}(\mathbf{k}') = \sum_{\mathbf{R}}^{N_R} t_{i0j\mathbf{R}} w_{\mathbf{R}} e^{+i\mathbf{k}'\cdot\mathbf{R}}. \qquad (51)$$

Here, $\mathbf{k}'$ is the k point employed in the band dispersion or the k point used in the Monkhorst–Pack mesh for the density of state calculation:

$$\{\mathbf{k}'\} = \begin{cases} \{\mathbf{k}_{\text{disp}}\}, & \text{for band-dispersion calculation,} \quad \text{(a)} \\ \{\mathbf{k}_{\text{MP}}\}, & \text{for density-of-state calculation.} \quad \text{(b)} \end{cases} \qquad (52)$$

Also, $w_{\mathbf{R}}$ in Eq. (51) is a weight factor at the lattice $\mathbf{R}$, which is introduced to avoid the double counting of the transfer at the boundary edge of the system with the periodic boundary condition. Note that $w_{\mathbf{R}}$ satisfies the following sum rule $\sum_{\mathbf{R}} w_{\mathbf{R}} = N_k$.

By diagonalizing the matrix $H_{ij}(\mathbf{k}')$,

$$\sum_j^{N_w} H_{ij}(\mathbf{k}')C_{j\alpha}(\mathbf{k}') = C_{i\alpha}(\mathbf{k}')\epsilon_{\alpha\mathbf{k}'}, \qquad (53)$$

we obtain eigenvectors $\{C_{j\alpha}(\mathbf{k}')\}$ and eigenvalues $\epsilon_{\alpha\mathbf{k}'}$. With $\epsilon_{\alpha\mathbf{k}'}$, we can calculate the density of state as

$$\rho(\omega) = \sum_i^{N_w} \rho_i(\omega) \qquad (54)$$

with

$$\rho_i(\omega) = \frac{2}{N_{k'}} \sum_{\mathbf{k}'}^{N_{k'}} \sum_{\alpha}^{N_w} |C_{i\alpha}(\mathbf{k}')|^2 \frac{1}{\pi} \text{Im} \frac{1}{\omega - \epsilon_{\alpha\mathbf{k}'} - i\delta} \qquad (55)$$

being the partial density of state associated with the Wannier orbital ϕ_{i0}. The factor of 2 comes from the sum over spin degrees of freedom. The Brillouin Zone integral is performed with the generalized tetrahedron technique [54,55].

As a similar quantity, a density matrix is calculated as follows:

$$D_{ij}(\mathbf{R}) = \frac{2}{N_k} \sum_{\mathbf{k}'}^{N_{k'}} \sum_{\alpha}^{N_w} C_{i\alpha}(\mathbf{k}') C_{j\alpha}^*(\mathbf{k}') e^{i\mathbf{k}' \cdot \mathbf{R}}$$

$$\times \frac{1}{\pi} \int_{-\infty}^{E_F} \frac{1}{\omega - \epsilon_{\alpha\mathbf{k}'} - i\delta} d\omega. \tag{56}$$

This is convenient to monitor occupancy of each Wannier orbital or bond order between the Wannier orbitals. The Fermi surface is also calculated as constant energy surface $F(\mathbf{k}')$

$$F(\mathbf{k}') \text{ to satisfy } \epsilon_{\alpha\mathbf{k}'} = E_F. \tag{57}$$

The output can be visualized by software FERMISURFER [60].

3.4. Parallel calculation

The polarization function can be calculated in parallel. There are two parallelization levels; one over the irreducible q points and the other over band pairs. First, let us consider the parallel calculation over the band pairs. To see this treatment, we rewrite the polarization function [Eq. (16)] as follows:

$$\chi_{\mathbf{G}\mathbf{G}'}(\mathbf{q}, \omega) = \sum_{\alpha}^{N_{vir}} \sum_{\beta}^{N_{occ}} \chi_{\mathbf{G}\mathbf{G}'}^{\alpha\beta}(\mathbf{q}, \omega). \tag{58}$$

The band sums are divided, and each $\chi_{\mathbf{G}\mathbf{G}'}^{\alpha\beta}(\mathbf{q}, \omega)$ can be calculated by an independent MPI process. Now, we write this process as follows:

$$\chi_{\mathbf{G}\mathbf{G}'}(\mathbf{q}, \omega) = \sum_{n}^{N_{MPI}} \sum_{m}^{N_{MPI}} \left\{ \sum_{\alpha_m}^{N_{vir}^m} \sum_{\beta_n}^{N_{occ}^n} \chi_{\mathbf{G}\mathbf{G}'}^{\alpha_m \beta_n}(\mathbf{q}, \omega) \right\}. \tag{59}$$

Here, n and m specify an index of a Message Passing Interface (MPI) process. The occupied-state and virtual-state data $\{\beta\}$ and $\{\alpha\}$ are divided into N_{MPI} processes; $(\{\beta_1\}, \ldots, \{\beta_{N_{MPI}}\})$ and $(\{\alpha_1\}, \ldots, \{\alpha_{N_{MPI}}\})$. The divided virtual-state data are interchanged among the MPI processes to compute the partial-sum contribution to the polarization function. MPI_SENDRECV routine is used for this data interchange.

Fig. 2 is a practical procedure for the case of $N_{MPI} = 2$. The occupied-state and virtual-state data are divided into two, and each data are stored in each MPI process (Step 1). After performing the polarization calculations in each MPI process (Step 2), only the virtual-state data $\{\alpha_1\}$ and $\{\alpha_2\}$ are interchanged between the two MPI processes (Step 3). Then, the polarization calculation is performed again (Step 4). Finally, the data stored in each MPI process is collected in the master process (Step 5).

A parallel calculation over the q points is more trivial. Consider the case where the total number of the MPI processes is 64, and the number of irreducible q points is 4. We first divide all the 64 MPI processes into 4 communities, and thus each community consists of 16 MPI processes. One community performs the polarization calculation of one q point. Fig. 3 is a schematic figure showing this procedure. MPI_COMM_SPLIT routine is used for splitting to the communities. The 16 MPI processes in each community are assigned to perform the parallel calculation over the band pairs mentioned above.

4. Calculation flow

We next describe the practical procedure of a RESPACK calculation [51]. Fig. 4 shows an overall flow diagram of calculation processes; first, we perform band-structure calculations with xTAPP [61] or QUANTUM ESPRESSO [62,63]. Next, with using the interface script, we convert the band-structure results to the
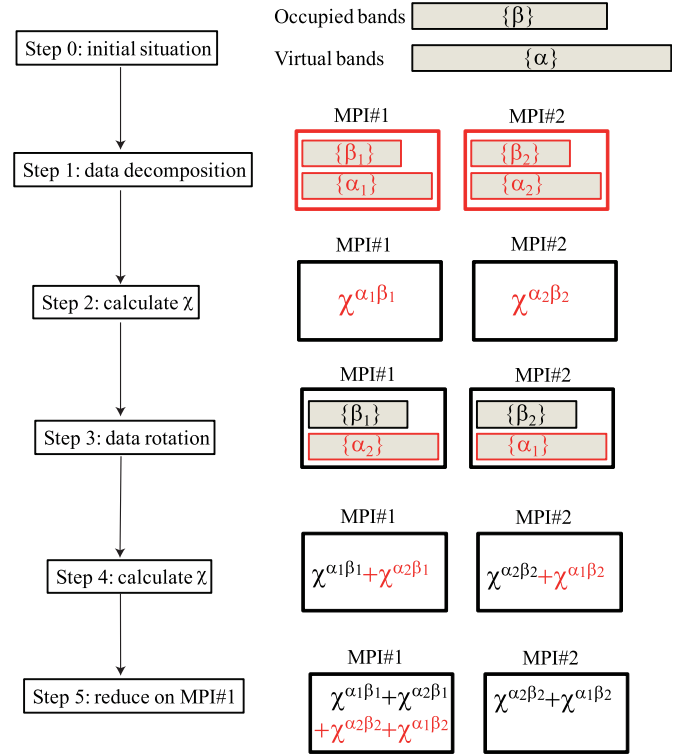
Fig. 2. Practical procedure for an Message Passing Interface (MPI) calculation of polarization function. On the right side, work images are displayed, and the work at each step is highlighted in red. In this example, the total number of the MPI processes is 2. The band data are divided into two and accommodated in each MPI process (step 1). After performing polarization calculations in each MPI process (step 2), only virtual data are interchanged among the MPI processes (step 3). The polarization calculations are performed again (step 4). Finally, the partial-sum data of the polarization functions stored in each MPI process are collected in the master node (step 5).

- ☐ Number of total MPI processes: 64
- ☐ Number of communities: 4
- ☐ Number of MPI processes per community: 16 (= 64 /4)
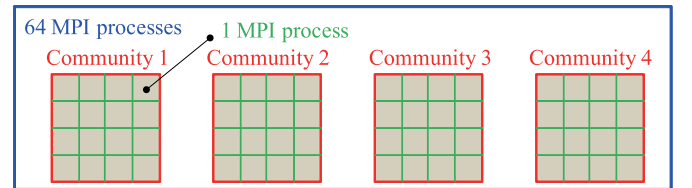
Fig. 3. Schematic diagram of a parallel computation on q points. In this example, the total number of Message Passing Interface (MPI) processes is 64. All the MPI processes are divided into 4 MPI communities with setting the q-point parallel degree to 4. Hence, each MPI community consists of 16 MPI processes which are allocated to the parallel calculation for the band pair.

inputs of RESPACK. Then, with the obtained band-calculation data and an input file that specifies the RESPACK-calculation condition, we perform the Wannier-function calculation. We call this calculation *wannier*. Then, we calculate the polarization and dielectric functions, and this calculation is called *chiqw*. In the constrained RPA, the polarization process is restricted by using the information of the Wannier function [see Eqs. (16) and (20)], so one has to perform the *wannier* calculation before the *chiqw* calculation. Lastly, with the *wannier* and *chiqw* outputs, we evaluate the matrix elements of the screened interaction. This calculation is called *calc_int*. In the following subsections, we describe details.
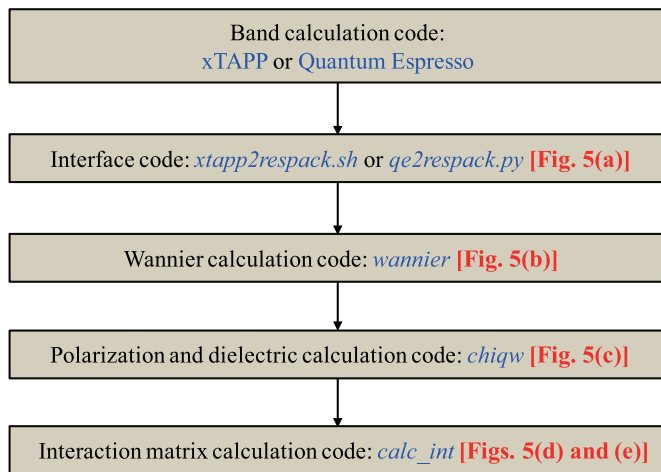
Fig. 4. Flow diagram of an *ab initio* derivation for an effective low-energy model in Eq. (1) with RESPACK. After the band calculations with xTAPP or Quantum Espresso, via an interface code, inputs of the RESPACK calculations are prepared. Lower three codes (*wannier*, *chqw*, and *calc_int*) compose the main part of RESPACK to derive the effective model.

4.1. Preparation for RESPACK

We show in Fig. 5(a) a preparation process from band-structure calculation with xTAPP or Quantum Espresso to RESPACK. In RESPACK, interface scripts that convert outputs of the band calculation to inputs for RESPACK are prepared for these two codes. In the case of xTAPP, xtapp2respack.sh generates a directory dir-wfn, in which the following 9 files are created.

1. dat.bandcalc (band calculation information)
2. dat.sample-k (sample *k* points)
3. dat.symmetry (symmetry operations)
4. dat.lattice (lattice vectors)
5. dat.eigenvalue (energy eigenvalues)
6. dat.nkm (number of reciprocal lattice vectors)
7. dat.wfn (wave functions)
8. dat.kg (reciprocal lattice vectors)
9. dat.atom_position (atomic positions)

For the format of each file, see the manual [51]. In the case of Quantum ESPRESSO, qe2respack.py is the generation script. After this process, RESPACK calculations are performed with the data in dir-wfn.

4.2. Wannier calculation

Fig. 5(b) is a flow diagram of *wannier*. With the data in dir-wfn and an input input.in that describes conditions of the *wannier* calculation, the calculation is performed with an executable file calc_wannier. Details of input.in are described in Appendix A. After the calculation, two directories dir-wan and dir-model are generated, in which the calculation results are saved. For details of the generated output files, see the descriptions in Fig. 5(b).

4.3. Chiqw calculation

We next show in Fig. 5(c) a flow diagram of *chiqw*. This code calculates the polarization and dielectric functions. With the data in dir-wfn and dir-wan and the input file input.in, the

calculation is performed with an executable file calc_chiqw. After the calculation, a directory dir-eps is generated and, under this directory, subdirectories q001, q002, …qNirr are generated, where 001, 002, and Nirr are the numbers of the irreducible *q* points. The calculation results of every *q* points are saved in each subdirectory.

4.4. Calc_int calculation

Figs. 5(d) and (e) show flow diagrams for the direct-Coulomb-integral and exchange-integral calculations, respectively. A common namelist &param_calc_int described in input.in can be used for the two calculation programs (see Table A.14). Executable files are calc_w3d for the direct-Coulomb integral and calc_j3d for the exchange integral. The calculation results are saved in the directories dir-intW, dir-intJ, and dir-model.

5. Installation instructions

5.1. Download source files and compile

The source code of RESPACK can be obtained from the official website https://sites.google.com/view/kazuma7k6r. A gzipped tar file RESPACK.tar.gz contains everything necessary for installation. When moving to the directory src, one finds three source directories: calc_int, chiqw, wannier. Makefile is prepared in each source directory, and one executes the make command to compile these source codes. In the case of chiqw, the work so far is as follows:

```
> tar -zxvf RESPACK.tar.gz
> cd RESPACK/src/chiqw/
> make
```

Here, > is a prompt character. After make, an executable file calc_chiqw is generated. This procedure is the same for the other programs. The verified Fortran 90 compilers for RESPACK are Intel Fortran and gfortran, and the verified MPI libraries for RESPACK are Open MPI and Intel MPI.

5.2. Compile using cmake

RESPACK can also be compiled using CMake. In CMake, one needs to make a temporary directory for compilation, and executes the cmake and make commands from that directory as follows:

```
> tar -zxvf RESPACK.tar.gz
> cd RESPACK
> mkdir build
> cd build
> cmake -DCONFIG=gcc
-DCMAKE_INSTALL_PREFIX=PATH_TO_INSTALL ../
> make
> make install
```

If make is successful, executable files are generated in each directory under RESPACK/build/src. By executing make install, the executable files will be installed in the bin directory under the directory specified by the -DCMAKE_INSTALL_PREFIX option. If the -DCMAKE_INSTALL_PREFIX option is omitted, it will be installed under /usr/local/bin. The -DCONFIG option is used for reading the CMake configuration files stored in the RESPACK/config directory. For -DCONFIG, the following options are available:
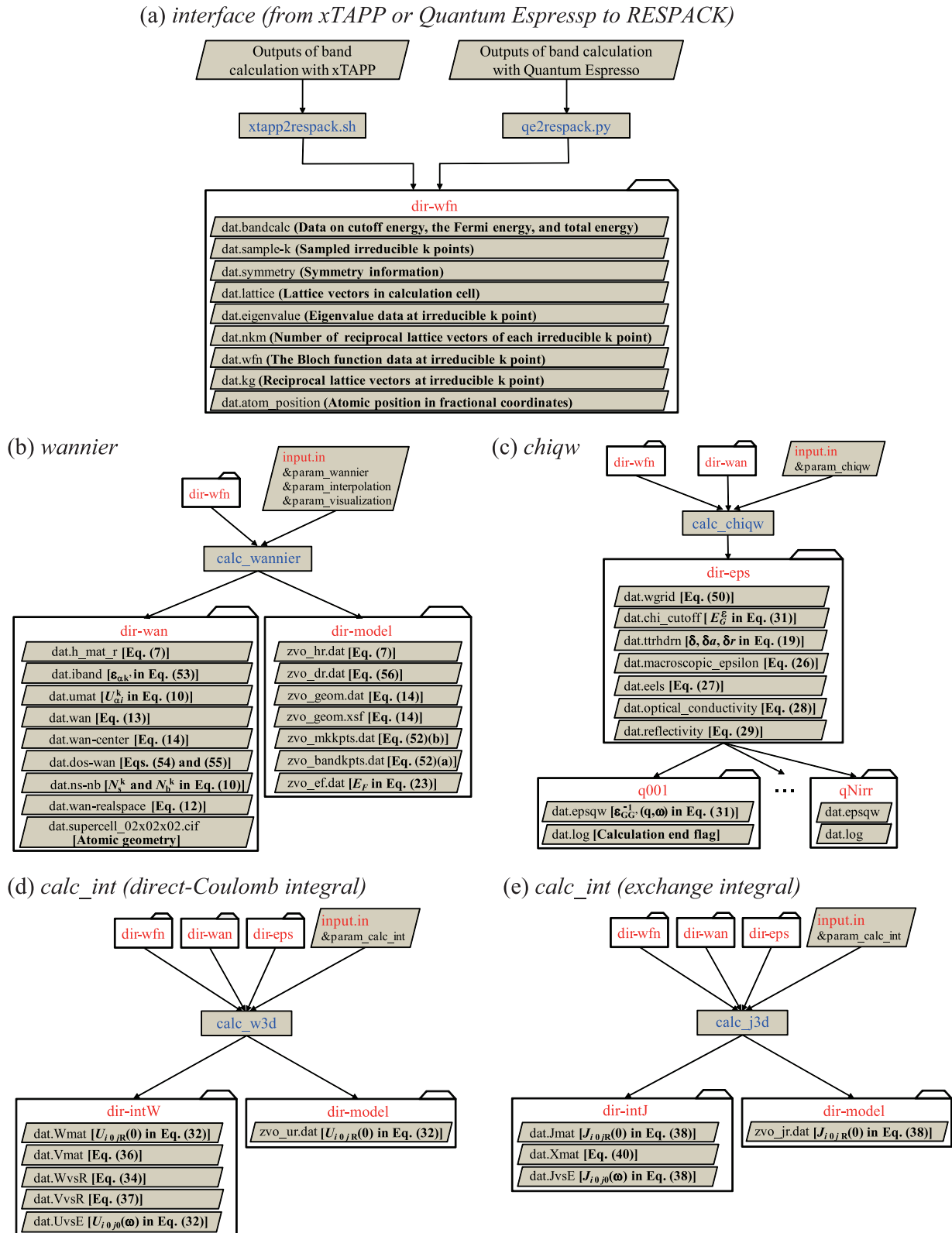
Fig. 5. Flow diagram of RESPACK. (a) Preparation process from DFT codes of xTAPP or QUANTUM ESPRESSO to RESPACK. The band-calculation results are converted to inputs of RESPACK with an interface program (xtapp2respack.sh for xTAPP and qe2respack.py for QUANTUM ESPRESSO). Nine files are generated in the directory dir-wfn. (b) *wannier* calculation: With the data in dir-wfn and input.in, the *wanner* calculation is performed with an executable file calc_wannier. The calculation results are stored in the directories dir-wan and dir-model. (c) *chiqw* calculation: With the data in dir-wfn and dir-wan and input.in, the *chiqw* calculation is performed with an executable file calc_chiqw. The calculation results are saved in the directories dir-eps and subdirectories q001, q002, ...qNirr. See text for details. (d) and (e) *calc_int* calculation [(d) direct-Coulomb integral and (e) exchange integral]. With the data in dir-wfn, dir-wan, and dir-eps and input.in, the *calc_int* calculation is performed with an executable file calc_w3d for the direct-Coulomb integrals and calc_j3d for the exchange integrals. The calculation results are stored in the directories dir-intW, dir-intJ, and dir-model.

- `intel`: Intel compiler
- `gcc`: GNU compiler

If one wants to execute the `cmake` command again, it is recommended that one deletes the temporary directory `build` and restart from scratch, because the previous settings may remain.

6. Benchmark

6.1. Typical outputs

In this section, we show benchmark results for a t_{2g}-model derivation of perovskite oxide $SrVO_3$ with a simple cubic structure having a lattice constant of 3.8425 Å. Density functional calculations with plane-wave basis sets were performed using the xTAPP code [61], where the norm-conserving pseudopotential [64,65] and the generalized gradient approximation to the exchange correlation energy were employed [66]. The calculation condition is set to $8 \times 8 \times 8$ k-point sampling, 100-Ry wavefunction cutoff, and 400-Ry charge-density cutoff. The 50 bands are considered for the polarization function, which corresponds to considering the excitation from the Fermi level to 35 eV. The numbers of the doubly-occupied, partially-occupied, and unoccupied bands are 12, 3, and 35, respectively.

Table 1 is an input file `input.in` for RESPACK calculations. Details of `input.in` are described in Appendix A. We construct the t_{2g}-type Wannier functions from the low-energy bands near the Fermi level. The calculations are performed with both of the constrained RPA and usual RPA to show the difference between these two. The cutoff for the polarization function is set to 10 Ry, and the broadening factor δ of the generalized tetrahedron calculation is set to 0.1 eV.

Fig. 6 is a comparison between the original KS band (red-solid curves) and the Wannier-interpolated band (green-dashed curves). A region between the two blue-dashed horizontal lines indicates the energy window used to construct the t_{2g}-type Wannier functions. We also show in Fig. 7 the calculated d_{xy} Wannier function in realspace.

We show in Fig. 8 important transfers for the t_{2g} band, where the definition and values of t_1, t_2, t_3, and t_4 are illustrated in Fig. 8. In this figure, we depict the d_{xy} Wannier function as an example. Since the lattice of the system is simple cubic, there exist equivalent transfers for the d_{yz} and d_{zx} orbitals. RESPACK provides a utility code that searches the equivalent transfers, which is described in Appendix B in more detail. We note that the original band structure in Fig. 6 is well reproduced by these four transfers.

Fig. 9 shows calculated macroscopic dielectric functions [Eq. (26)] with the RESPACK-*chiqw* code. Panels (a) and (b) describe the constrained RPA and usual RPA results, respectively. Red-solid and green-dashed curves describe the real and imaginary parts, respectively, and circles represent calculation values. The difference between the constrained RPA and usual RPA spectra is appreciable in the low-energy excitation region less than 2–3 eV. In the constrained RPA, a metallic charge excitation is excluded by the polarization constraint described in Section 2.3, and then the real part of $\epsilon_M(\omega)$ converges to the finite value in the $\omega \to 0$ limit, while, in the usual RPA, the real part of $\epsilon_M(\omega)$ diverges negatively due to the metallic charge excitation [68], thus leading to the Drude behavior of the imaginary part of $\epsilon_M(\omega)$.

It should be noted here that the present spectra neglect the transition moment contributed from the commutation relation between the non-local pseudopotential and electronic position, $[V_{NL}, \mathbf{r}]$, in Eq. (24). For transition metals, this contribution is known to affect the spectral property in the low-energy excitation region [58]. In the present $SrVO_3$, we checked that this contribution is not significant [69]. An evaluation method based on the
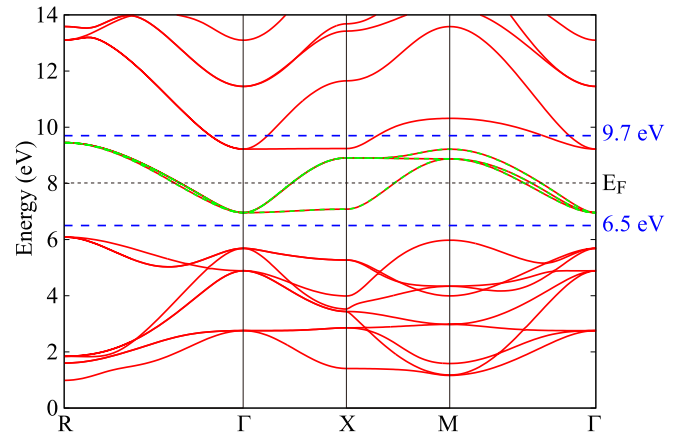
Fig. 6. Calculated band structure for $SrVO_3$. Red-solid curve is DFT band dispersion by xTAPP and green-dashed curve is the Wannier-interpolated t_{2g}-band dispersion with RESPACK-*wannier* code. A region between the two blue-dashed horizontal lines indicates the energy window region, and the band structure data in this region is used for constructing the Wannier functions. The dotted horizontal line is the Fermi level as 8.02 eV. Dispersions are plotted along the high-symmetry points, where R=$\frac{1}{2}\boldsymbol{a}^* + \frac{1}{2}\boldsymbol{b}^* + \frac{1}{2}\boldsymbol{c}^*$, $\Gamma = \mathbf{0}$, X=$\frac{1}{2}\boldsymbol{a}^*$, and M=$\frac{1}{2}\boldsymbol{a}^* + \frac{1}{2}\boldsymbol{b}^*$ with $\boldsymbol{a}^*$, $\boldsymbol{b}^*$, and $\boldsymbol{c}^*$ being basis vectors of reciprocal lattice, respectively. In the simple cubic primitive lattice, $\boldsymbol{a}^* = \frac{2\pi}{a}\hat{x}$, $\boldsymbol{b}^* = \frac{2\pi}{a}\hat{y}$, and $\boldsymbol{c}^* = \frac{2\pi}{a}\hat{z}$ with $\hat{x}$, $\hat{y}$, and $\hat{z}$ being unit vectors of the Cartesian coordinates. Also, a is a lattice constant of 3.8425 Å. The root mean square error between the DFT and Wannier-interpolated bands was found to be 0.00163 eV.
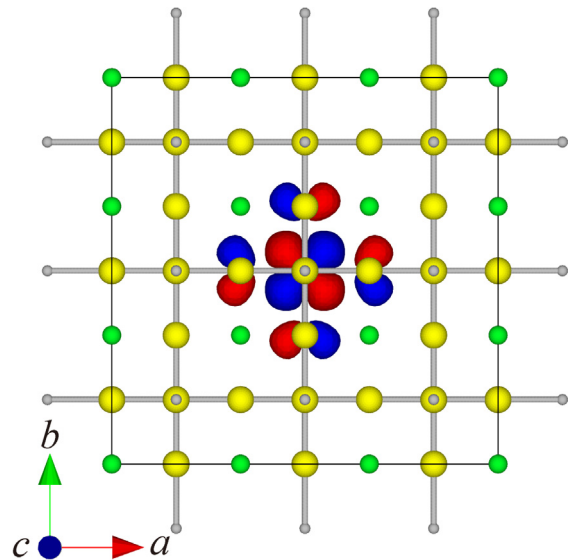
Fig. 7. Calculated realspace d_{xy}-type Wannier function of $SrVO_3$ with the RESPACK-*wannier* code (drawn by VESTA [67]). Blue and red contour plots indicate positive- and negative-value region of the Wannier function. Large-yellow, middle-green, and small-gray spheres are oxygen, strontium, and vanadium atoms, respectively. In the simple cubic primitive lattice, $\boldsymbol{a} = a\hat{x}$, $\boldsymbol{b} = a\hat{y}$ and $\boldsymbol{c} = a\hat{z}$. (For interpretation of the references to color in this figure legend, the reader is referred to the web version of this article.)

Wannier basis has also been proposed in Ref. [70]. Support for this contribution is a future issue in the RESPACK project.

We next show in Fig. 10 other optical properties calculated with the usual RPA and constrained RPA. Panels (a), (b), and (c) display EELS $L(\omega)$ [Eq. (27)], the real part of the optical conductivity $\sigma(\omega)$ [Eq. (28)], and the reflectance spectrum $R(\omega)$ [Eq. (29)], respectively. Red-solid and green-dashed curves represent the results based on the usual RPA and constrained RPA, respectively.

Table 1

Input file `input.in` for a RESPACK calculation. This input describes a derivation of parameters specifying an effective low-energy model for the t_{2g} band of SrVO₃. &param_wannier, &param_interpolation, and &param_visualization specify the namelists for the *wannier* calculation [see Fig. 5(b) and details are described in Appendices A.1, A.2, and A.3]. &param_chiqw is the namelist for the *chiqw* calculation [Fig. 5(c) and Appendix A.4]. &param_calc_int is the namelist for the *calc_int* calculation [Figs. 5(d) and (e) and Appendix A.5]. A brief description of each variable is given in the right of !. Default values are shown with a bold font in parentheses. A variable that does not include a bold-font value is a required variable.

```
&param_wannier
N_wannier=3, ! Number of the Wannier functions you want to calculate
Lower_energy_window=6.50, ! Lower bound of energy window
Upper_energy_window=9.70, ! Upper bound of energy window
N_initial_guess=3, ! Number of initial guesses
/
dxy 0.50 0.50 0.50 0.50 ! vec_ini(1)%orb vec_ini(1)%a vec_ini(1)%x vec_ini(1)%y vec_ini(1)%z
dyz 0.50 0.50 0.50 0.50 ! vec_ini(2)%orb vec_ini(2)%a vec_ini(2)%x vec_ini(2)%y vec_ini(2)%z
dzx 0.50 0.50 0.50 0.50 ! vec_ini(3)%orb vec_ini(3)%a vec_ini(3)%x vec_ini(3)%y vec_ini(3)%z


&param_interpolation
N_sym_points=5, ! Number of symmetric k points in calculation lines for band dispersion
/
0.50 0.50 0.50 ! SK_sym_pts(1,1) SK_sym_pts(2,1) SK_sym_pts(3,1): R
0.00 0.00 0.00 ! SK_sym_pts(1,2) SK_sym_pts(2,2) SK_sym_pts(3,2): Gamma
0.50 0.00 0.00 ! SK_sym_pts(1,3) SK_sym_pts(2,3) SK_sym_pts(3,3): X
0.50 0.50 0.00 ! SK_sym_pts(1,4) SK_sym_pts(2,4) SK_sym_pts(3,4): M
0.00 0.00 0.00 ! SK_sym_pts(1,5) SK_sym_pts(2,5) SK_sym_pts(3,5): Gamma


&param_visualization
Flg_vis_wannier=1, ! Calculate realspace Wannier function (do not: 0, do: 1) (0)
/


&param_chiqw
Ecut_for_eps=10.0, ! Cutoff energy for polarization function in Rydberg unit (1/10 of wave-function cutoff)
Num_freq_grid=70, ! Number of frequency grid (70)
Green_func_delt=0.1, ! Smearing value used in tetrahedron calculation (eV) (0.1 eV)
MPI_num_qcomm=1, ! Degree of parallelism for q-point parallel calculation (1)
Flg_cRPA=1, ! Flag for constrained RPA or usual RPA (usual RPA: 0, constrained RPA: 1) (0)
/


&param_calc_int
Calc_ifreq=1, ! Number of frequency to output (1)
/
```
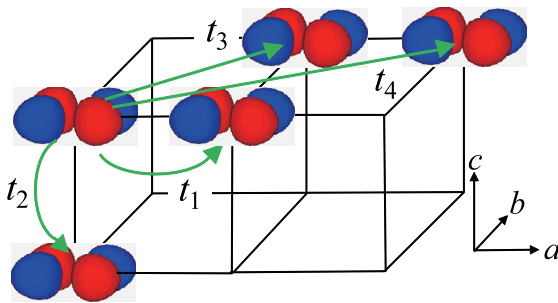

Fig. 8. Derived transfer parameters of a t_{2g} model of SrVO₃ as the Wannier matrix elements for the Kohn–Sham Hamiltonian in Eq. (2), where we show main 4 transfer integrals. The values of t_1, t_2, t_3, and t_4 are −0.259 eV, −0.026 eV, −0.086 eV, and −0.012 eV, respectively. In this figure, we depict the d_{xy}-type Wannier orbital. Equivalent transfers exist for the d_{yz}- and d_{zx}-type Wannier orbitals. These four transfers successfully reproduce the original t_{2g}-band structure in Fig. 6.

Circles denote the calculation values. There is a difference between the constrained RPA and usual RPA in the EELS around the low-energy excitation region less than 2 eV; in the usual RPA case, an additional peak appears in $L(\omega)$, which is due to the low-energy plasmon excitation in the t_{2g} band [71,72]. This plasma excitation is also observed in the reflectance spectrum $R(\omega)$; we see a sharp drop from around 1 to 0 in the RPA reflectance spectrum. On the optical conductivity, the spectral trend is basically the same as the macroscopic dielectric function $\epsilon_M(\omega)$; the usual RPA spectrum exhibits the Drude behavior characteristic of a metallic system in the low-excitation region less than 2 eV, while

the constrained RPA spectrum has no intensity in this frequency region, which is a characteristic aspect of the insulating system.

We show in Fig. 11 comparison between the theoretical and experimental results. Panels (a), (b), and (c) display EELS $L(\omega)$, the real part of the optical conductivity $\sigma(\omega)$, and the reflectance spectrum $R(\omega)$, respectively. Black-solid curves and green circles represent our calculations by RESPACK and experimental results taken from Ref. [72], respectively. About the optical conductivity, we also compare our result with other theoretical ones, where blue-cross and purple-plus data are taken from Refs. [73] and [74], respectively. Basically, our calculations are consistent with the previous theoretical results and reproduce the experimental results reasonably. On the other hand, if we look at the comparison with the experiments in more detail, the theoretical low-energy plasma frequency near 1.8 eV is slightly overestimated from the experimental one near 1.4 eV by the EELS and reflectance data. Also, about the optical conductivity, the theoretical intensities around 2–4 eV overestimate the experimental ones. These overestimation may be due to the lack of local electronic-correlation effects which are not included in the present DFT-based calculation [74].

We next show in Fig. 12 a distance dependence of the static ($\omega = 0$) direct-Coulomb integral [Eq. (34) for screened interaction and Eq. (37) for bare interaction], where the distance between the Wannier functions are defined by Eq. (35). Red crosses, green-open circles, and blue dots represent the bare, constrained-RPA, and RPA results, respectively. Solid and dashed curves are $1/r$ and $1/(\epsilon_0 r)$ with $\epsilon_0 = 6$, respectively.

Fig. 13 shows a frequency dependence of the onsite direct-Coulomb integral [$U_{1010}(\omega)$ in Eq. (32) with orbital index 1 denoting d_{xy}-type orbital]. Panels (a) and (b) represent the constrained
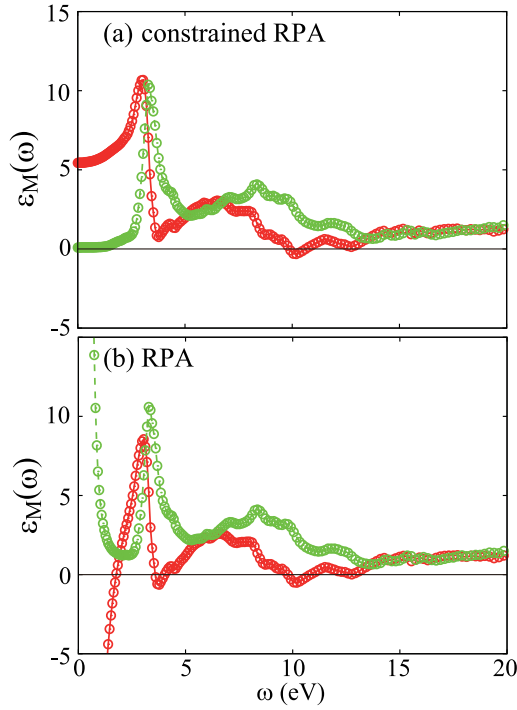
Fig. 9. Calculated macroscopic dielectric function in Eq. (26) of SrVO$_3$ with the RESPACK-*chiqw* code: (a) constrained RPA and (b) usual RPA. Circles represent calculation values, and the red-solid and green-dashed curves describe the real and imaginary parts of the spectra, respectively. (For interpretation of the references to color in this figure legend, the reader is referred to the web version of this article.)

RPA and usual RPA results, respectively. Red-solid and green-dashed curves describe the real and imaginary parts, respectively. As well as the optical data, the difference between the constrained RPA and usual RPA occurs in the low-energy excitation region below 2 eV due to the low-energy plasmon excitation considered in the usual RPA calculation.

Fig. 14 is a frequency dependence of the onsite exchange integral. [$J_{1020}(\omega)$ in Eq. (38) with orbital indices 1 and 2 denoting d_{xy}-type and d_{yz}-type orbitals, respectively]. In exchange integral, differences between the constrained RPA (a) and usual RPA (b) can also be observed around $\omega \sim 2$ eV.

6.2. Convergence check to calculation conditions

We next show a convergence behavior of the calculated interaction parameters of the t_{2g} model of SrVO$_3$ with respect to the various computational conditions. Table 2 shows a convergence of the static interaction parameters with increasing the sampling k-point density, where we list the static onsite-intraorbital interaction U, onsite-interorbital U', onsite-exchange J, and nearest-neighbor V interactions averaged over orbitals. We see that the convergence is achieved around $8 \times 8 \times 8$.

Table 3 is a dependence of the static interaction parameters of SrVO$_3$ on the total number of bands. We see that the 50 bands are enough to obtain the converged results.

Table 4 gives a convergence behavior of the static interaction parameters with respect to the cutoff energy E_{cut}^{ϵ} of the polarization function. This parameter is important for the convergence and it is desirable to take large enough. The convergence within 0.01 eV of the onsite constrained-RPA interaction parameters requires about 30 Ry, and in the case of the RPA parameter, it
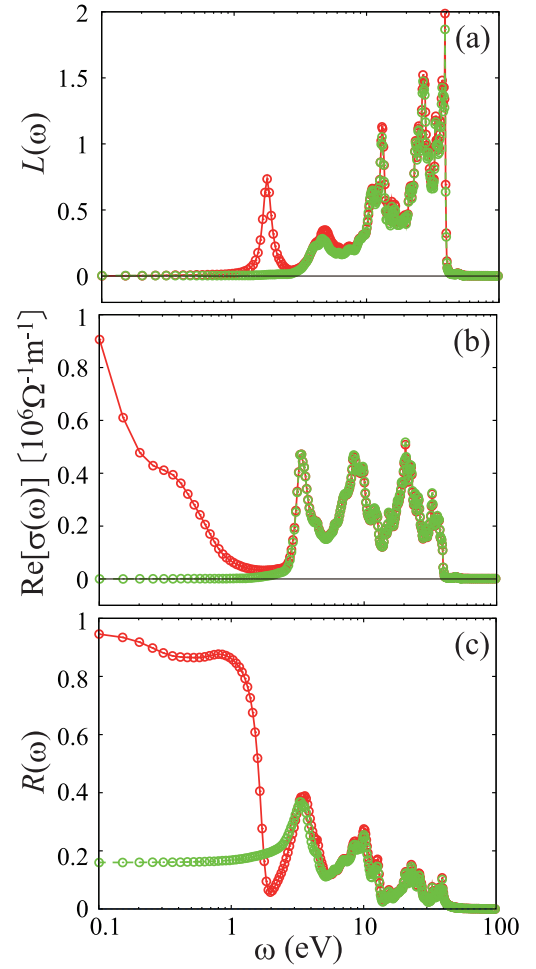
Fig. 10. Calculated optical properties of SrVO$_3$ with the RESPACK-*chiqw* code. (a) EELS $L(\omega)$ in Eq. (27), (b) the real part of the optical conductivity $\sigma(\omega)$ in Eq. (28), (c) reflectance spectrum $R(\omega)$ in Eq. (29). Circles represent calculation values, and the red-solid and green-dashed curves describe the usual RPA and the constrained RPA results, respectively. (For interpretation of the references to color in this figure legend, the reader is referred to the web version of this article.)

Table 2
Dependence of the static (ω=0) interaction parameters of the t_{2g} model of SrVO$_3$ on the sampling k-point density. The interaction parameters with the bare (unscreened), constrained RPA (cRPA), and usual RPA are listed. $V = (1/N_w)^2 \sum_{i,j=1}^{N_w} U_{i0j\mathbf{R}}$ is the orbital-averaged value of the nearest-neighbor interactions with $\mathbf{R} = (1, 0, 0)$. Other conditions are as follows: The total number of the bands $N_{band} = 50$, the cutoff energy for the polarization function $E_{cut}^{\epsilon} = 10$ Ry, and the broadening factor introduced in the *chiqw* calculation $\delta = 0.1$ eV. The unit of the interaction parameter is eV.

k^3	U			U'			J			V		
	bare	cRPA	RPA	bare	cRPA	RPA	bare	cRPA	RPA	bare	cRPA	RPA
5^3	15.12	3.37	1.25	13.83	2.26	0.27	0.60	0.53	0.48	3.56	0.65	0.01
6^3	15.16	3.38	1.30	13.87	2.26	0.30	0.60	0.53	0.48	3.57	0.65	0.01
7^3	15.20	3.42	1.30	13.91	2.30	0.31	0.60	0.53	0.48	3.59	0.67	0.02
8^3	15.22	3.50	1.21	13.93	2.38	0.24	0.60	0.53	0.47	3.60	0.71	0.02
9^3	15.23	3.47	1.24	13.94	2.35	0.26	0.60	0.53	0.47	3.61	0.70	0.02
10^3	15.24	3.46	1.26	13.96	2.35	0.28	0.60	0.53	0.48	3.62	0.70	0.02
11^3	15.26	3.47	1.26	13.97	2.35	0.28	0.60	0.53	0.48	3.63	0.70	0.02
12^3	15.27	3.49	1.25	13.98	2.37	0.27	0.60	0.53	0.48	3.64	0.71	0.02

is about 40 Ry. However, the large E_{cut}^{ϵ} needs the large computational time because of the double-loop calculation on the **G** and **G'** vectors in Eq. (16). By default, E_{cut}^{ϵ} is set to $E_{cut}^{\psi}/10$.
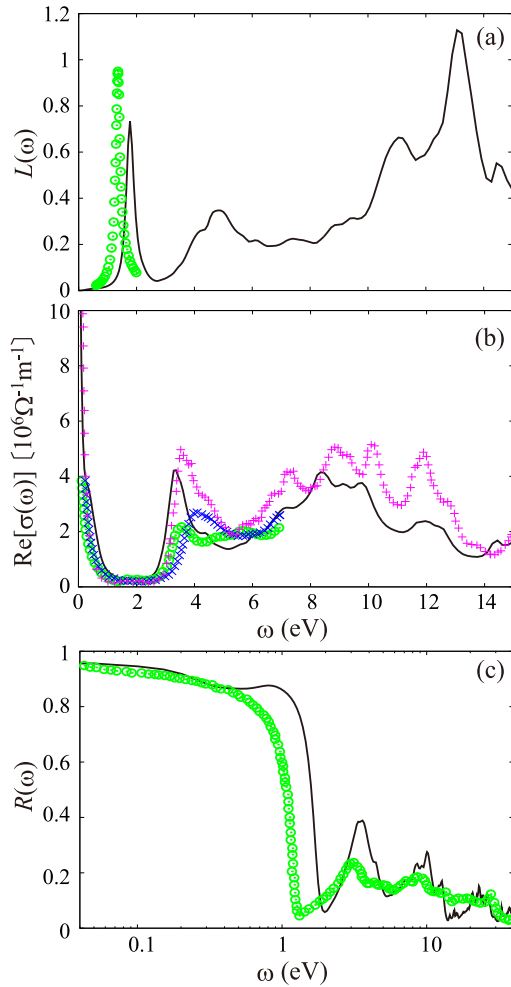
Fig. 11. Comparison between theoretical and experimental optical properties of SrVO₃. (a) EELS $L(\omega)$ in Eq. (27), (b) the real part of the optical conductivity $\sigma(\omega)$ in Eq. (28), (c) reflectance spectrum $R(\omega)$ in Eq. (29). Black-solid curves and green circles represent our calculated and experimental results [72], respectively. In the panel (b), we also compare our spectrum with other theoretical results, where blue-cross and purple-plus data are taken from Refs. [73] and [74], respectively.
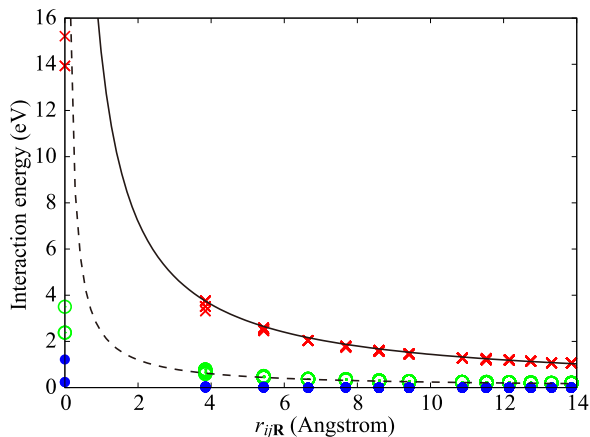
Fig. 12. Dependence of direct-Coulomb integral on distance between t_{2g} Wannier orbitals of SrVO₃ [Eqs. (34) and (37)], calculated with RESPACK-*calc_int* code. Red crosses, green-open circles, and blue dots represent the bare, constrained-RPA, and usual RPA results, respectively. Solid and dashed curves are $1/r$ and $1/(\epsilon_0 r)$ with $\epsilon_0 = 6$, respectively.
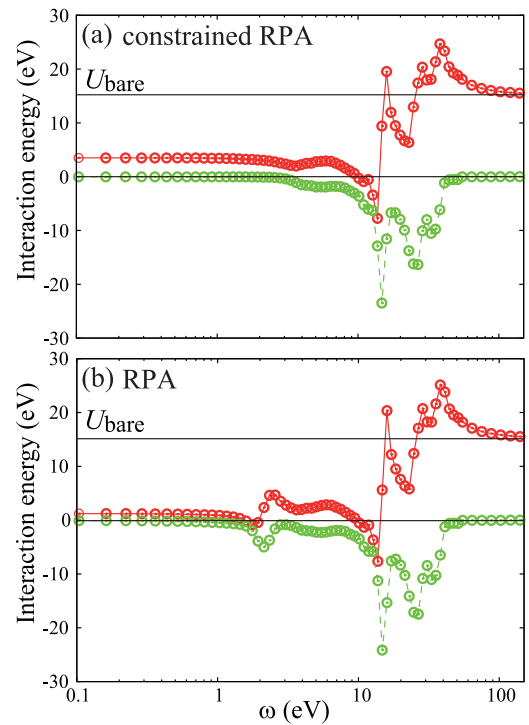
Fig. 13. Frequency dependence of onsite direct-Coulomb integral of SrVO₃ [$U_{d_{xy}\mathbf{0},d_{xy}\mathbf{0}}(\omega)$ in Eq. (32)], calculated with RESPACK-*calc_int* code. (a) constrained RPA and (b) usual RPA. Circles represent calculation values, and the red-solid and green-dashed curves describe the real and imaginary parts of the spectra, respectively. (For interpretation of the references to color in this figure legend, the reader is referred to the web version of this article.)
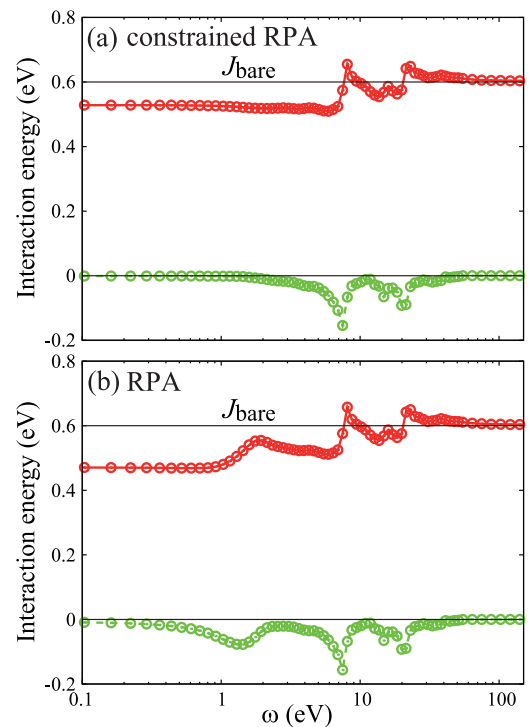
Fig. 14. Frequency dependence of onsite exchange integral of SrVO₃ [$J_{d_{xy}\mathbf{0},d_{yz}\mathbf{0}}(\omega)$ in Eq. (38)], calculated with RESPACK-*calc_int* code. (a) constrained RPA and (b) usual RPA. Circles represent calculation values, and the red-solid and green-dashed curves describe the real and imaginary parts of the spectra, respectively. (For interpretation of the references to color in this figure legend, the reader is referred to the web version of this article.)

Table 3

Dependence of the static (ω=0) interaction parameters of SrVO$_3$ on the total number of calculated bands N_{band}. The view of the table is the same as Table 2. Other conditions are as follows: $8 \times 8 \times 8$ k-grid, $E_{cut}^{\epsilon} = 10$ Ry, $\delta = 0.1$ eV. The unit of the interaction parameter is eV.

N_{band}	U		U'		J		V	
	cRPA	RPA	cRPA	RPA	cRPA	RPA	cRPA	RPA
30	3.59	1.22	2.45	0.24	0.53	0.47	0.73	0.02
50	3.50	1.21	2.38	0.24	0.53	0.47	0.71	0.02
100	3.47	1.21	2.36	0.24	0.53	0.47	0.70	0.02
150	3.46	1.21	2.36	0.24	0.52	0.47	0.70	0.02
200	3.46	1.21	2.36	0.24	0.52	0.47	0.70	0.02

Table 4

Dependence of the static (ω=0) interaction parameters of SrVO$_3$ on the cutoff energy E_{cut}^{ϵ} of the polarization function. The view of the table is the same as Table 2. Other conditions are as follows: $8 \times 8 \times 8$ k-grid, $N_{band} = 50$, $\delta = 0.1$ eV. The units are in Rydberg for E_{cut}^{ϵ} and eV for interaction parameters.

E_{cut}^{ϵ}	U		U'		J		V	
	cRPA	RPA	cRPA	RPA	cRPA	RPA	cRPA	RPA
5	3.64	1.47	2.45	0.32	0.57	0.56	0.70	0.02
10	3.50	1.21	2.38	0.24	0.53	0.47	0.71	0.02
15	3.50	1.13	2.40	0.26	0.50	0.41	0.71	0.02
20	3.46	1.04	2.39	0.25	0.49	0.37	0.71	0.02
25	3.44	0.98	2.38	0.24	0.48	0.35	0.71	0.02
30	3.43	0.94	2.38	0.23	0.48	0.33	0.71	0.02
35	3.42	0.91	2.37	0.23	0.48	0.32	0.71	0.02
40	3.42	0.89	2.37	0.23	0.48	0.31	0.71	0.02

Table 5

Dependence of static (ω=0) interaction parameters of SrVO$_3$ on the broadening factor δ in the polarization-function calculation in Eqs. (16), (18), and (19). The view of the table is the same as Table 2. Other conditions are as follows: $8 \times 8 \times 8$ k-grid, $N_{band} = 50$, $E_{cut}^{\epsilon} = 10$ Ry. The units of δ and the interaction parameter are eV.

δ	U		U'		J		V	
	cRPA	RPA	cRPA	RPA	cRPA	RPA	cRPA	RPA
0.001	3.50	1.19	2.38	0.22	0.53	0.47	0.71	0.02
0.005	3.50	1.19	2.38	0.22	0.53	0.47	0.71	0.02
0.01	3.50	1.19	2.38	0.23	0.53	0.47	0.71	0.02
0.05	3.50	1.20	2.38	0.23	0.53	0.47	0.71	0.02
0.1	3.50	1.21	2.38	0.24	0.53	0.47	0.71	0.02
0.2	3.50	1.23	2.38	0.25	0.53	0.47	0.71	0.02

Table 6

Dependence of bare (unscreened) interaction parameters of SrVO$_3$ on pseudopotential, where we change the r_{loc} parameter which is a cutoff radius for the local pseudopotential. In this table, we also list the Wannier spread in Eq. (15). Note that the pseudopotentials with r_{loc} = 0.8, 1.0, and 1.5 bohr are constructed for the semicore configuration and those with r_{loc} = 1.8 and 2.1 bohr are constructed for the valence configuration (see the text). Calculation condition is $8 \times 8 \times 8$ k-point sampling and 196-Ry wavefunction cutoff. The unit of the interaction parameter is eV.

r_{loc} [bohr]	S [Å^2]	U_{bare}	U'_{bare}	J_{bare}	V_{bare}
0.8	1.88490	16.13	14.92	0.57	3.60
1.0	1.88735	16.13	14.91	0.58	3.60
1.5	1.89448	15.91	14.65	0.60	3.60
1.8	1.96969	15.59	14.31	0.60	3.60
2.1	1.97853	15.21	13.92	0.60	3.60

Table 5 is a dependence of the static onsite interaction parameter on the broadening factor δ introduced in the polarization-function calculation of Eqs. (16), (18), and (19). We see that the δ does not affect the static cRPA and RPA results.

We note that the δ may affect dynamical properties, especially in the low-energy collective excitation. Fig. 15 is the δ dependence of EELS function $L(\omega)$ in Eq. (27). As the δ value increases [0.001 eV (black curves), 0.01 eV (purple curves), 0.05 eV (blue curves), 0.1 eV (green curves), and 0.2 eV (red curves)],
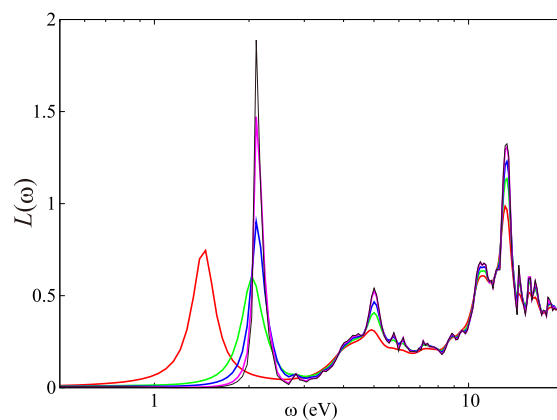
Fig. 15. Dependence of EELS function $L(\omega)$ in Eq. (27) of SrVO$_3$ on the broadening factor δ introduced in the polarization-function calculation [Eqs. (16), (18), and (19)]. The calculation is based on the usual RPA. The spectra drawn by black, purple, blue, green, and red indicate the spectra with δ = 0.001 eV, 0.01 eV, 0.05 eV, 0.1 eV, and 0.2 eV, respectively. A spectral behavior around 1–2 eV results from the plasmon excitation within the t_{2g} band. As the δ increases, the peak intensity decreases and the peak position shifts to the lower-energy side eventually. (For interpretation of the references to color in this figure legend, the reader is referred to the web version of this article.)

the intensity of the plasmon peak around 1–2 eV decreases and eventually the peak position shifts to the lower energy. The plasma excitation is also sensitive to the k-point density [57]. Therefore, one should be careful about computational conditions for the quantitative discussion of the dynamical properties.

6.3. Pseudopotential dependence

Here, we discuss the pseudopotential dependence of the interaction parameters in details. The pseudopotential depends mainly on the cutoff radius r_{loc} for local pseudopotential. The pseudopotential with a small r_{loc} parameter makes deeper potential, and the resulting pseudo wavefunction tends to be more localized near the ion core. We constructed the five pseudopotentials with the different r_{loc} values (0.8, 1.0, 1.5, 1.8 and 2.1 bohr) for a vanadium atom. The pseudopotential with r_{loc} = 0.8, 1.0, and 1.5 bohr were constructed for an ionic semicore configuration of $(3s)^2(3p)^6(3d)^3$. The pseudopotentials with r_{loc} = 1.8 and 2.1 bohr were constructed with an ionic valence configuration of $(3d)^3(4s)^0(4p)^0$. The Troullier–Martins (TM) type was adopted as a function form of the pseudo wavefunction [65]. $8 \times 8 \times 8$ k-point sampling and wavefunction cutoff E_{cut}^{ψ} of 196 Ry are employed. The total number of bands N_{band} is 50, and the broadening factor δ was set to be 0.1 eV. A polarization-function cutoff E_{cut}^{ϵ} is important for the effective interaction parameters, so the convergence behavior is discussed for this parameter. We note that the t_{2g}-band structures obtained with the above 5 pseudopotentials are in almost perfect agreements.

Fig. 16 compares the atomic pseudo wavefunctions obtained with the different r_{loc} parameters with the atomic all-electron wavefunction (black curve). As the r_{loc} parameter is reduced from 2.1 bohr (light blue) → 1.8 bohr (purple) → 1.5 bohr (blue) → 1.0 bohr (green) → 0.8 bohr (red), the maximum amplitude position of the pseudo wavefunction is shifted to the ion-core side. The pseudo wavefunctions with the r_{loc} = 0.8 and 1.0 bohr are almost the same as the all-electron wave function.

This trend can affect the localization of the Wannier function; the Wannier function generated with a pseudopotential with a small r_{loc} cutoff tends to be more localized. As a result, it can give a large bare (unscreened) direct-Coulomb integral. Table 6 shows the r_{loc} dependence of the bare interaction parameters for
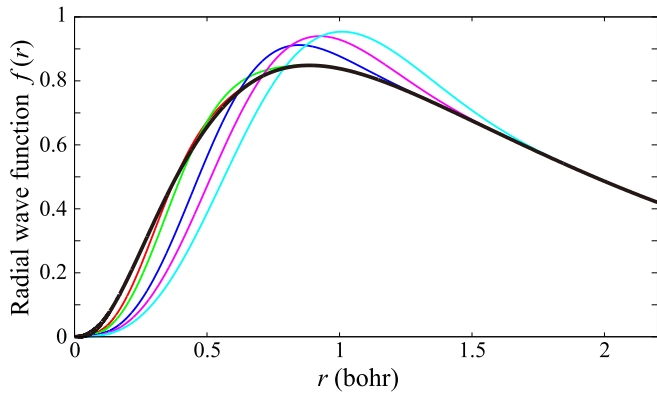
Fig. 16. Comparison of radial part of pseudo wavefunction and all-electron wavefunction (thick black curve) of the 3d orbital of a vanadium atom. The figure compares the pseudo wavefunctions obtained with different pseudopotentials, where a cutoff radius of the local pseudopotential r_{loc} is changed. Red, green, blue, purple, and light-blue curves are the results with r_{loc} = 0.8, 1.0, 1.5, 1.8, and 2.1 bohr, respectively. By reducing the r_{loc} parameter, the maximum-amplitude position of the pseudo wavefunction is shifted to the ion-core side ($r = 0$). (For interpretation of the references to color in this figure legend, the reader is referred to the web version of this article.)

the t_{2g} Wannier function of SrVO$_3$. We see from the table that the r_{loc} and the Wannier spread S_{i0} in Eq. (15) have clear positive correlation; a smaller r_{loc} leads to a smaller Wannier spread. As a result, the r_{loc} and bare onsite direct-Coulomb integrals U_{bare} and U'_{bare} correlate negatively (i.e., the small r_{loc} brings about the large U_{bare} and U'_{bare}). There are no discernible effects on the bare exchange J_{bare} and the bare nearest-neighbor direct integrals V_{bare}.

Tables 7 is the pseudopotential dependence of constrained-RPA and usual-RPA interaction parameters. An interesting trend can be seen in the table; details of the pseudopotential hardly affect the interaction values in contrast to the bare (unscreened) interaction parameters. In general, however, sufficiently large E_{cut}^{ϵ} would be desirable for a safer quantitative discussion about effective interaction parameters, especially for the usual RPA case.

Finally, we mention the effects of the pseudopotential type. As the famous pseudopotential types, besides the TM type, there are the ONCV (Optimized Norm-Conserving Vanderbilt) type [75] and the RRKJ (Rappe-Rabe-Kaxiras-Joannopoulos) type [76]. Even if the same cutoff r_{loc} is employed, the results can be quantitatively different due to the difference in the functional form of the pseudopotential, so the user should be careful about this point. Table 8 compares the calculated interaction parameters based on the TM-type, ONCV-type [77] and RRKJ-type [78] pseudopotentials. The calculations with the TM-type pseudopotential were performed with xTAPP, which is referred to as TM-xTAPP. The calculations with the ONCV-type and RRKJ-type pseudopotentials were performed with QUANTUM ESPRESSO, which are referred to as ONCV-QE and RRKJ-QE, respectively. For the TM-xTAPP, we give two results TM(v)-xTAPP and TM(s)-xTAPP, for which the former is the results based on the pseudopotential constructed with the valence-electron configuration, and the latter is the results based on the pseudopotential with the semicore configuration for V and Sr. The ONCV and RRKJ pseudopotentials are also constructed for the semicore configurations for V and Sr. We found that, for the screened direct-Coulomb interaction U and U', RRKJ-QE gives significantly smaller values than others.

6.4. Parallelization performance

In this subsection, we discuss the parallelization performance of RESPACK. The parallelization is important when dealing with

Table 7
Dependence of static (ω=0) interaction parameters of SrVO$_3$ on pseudopotential, where we change the r_{loc} parameter which is a cutoff radius for the local pseudopotential. Note that the pseudopotentials with r_{loc} = 0.8, 1.0, and 1.5 bohr are constructed for the semicore configuration and those with r_{loc} = 1.8 and 2.1 bohr are constructed for the valence configuration (see the text). Under each pseudopotential, the E_{cut}^{ϵ} cutoff dependence on the interaction parameters is investigated. Other calculation condition is as follows: $8 \times 8 \times 8$ k-point sampling, $N_{band} = 50$, $E_{cut}^{\psi} = 196$ Ry, and $\delta = 0.1$ eV. The unit of the interaction parameter is eV.

$r_{loc} = 0.8$ bohr	U		U'		J		V	
E_{cut}^{ϵ} [Ry]	cRPA	RPA	cRPA	RPA	cRPA	RPA	cRPA	RPA
5	3.85	1.62	2.73	0.52	0.54	0.53	0.66	0.02
10	3.53	1.19	2.46	0.23	0.52	0.47	0.67	0.02
15	3.51	1.09	2.46	0.22	0.50	0.42	0.68	0.02
20	3.49	1.03	2.47	0.23	0.48	0.38	0.68	0.02
25	3.48	0.99	2.48	0.24	0.47	0.36	0.68	0.02
30	3.47	0.96	2.48	0.24	0.47	0.34	0.68	0.02
35	3.47	0.94	2.48	0.25	0.47	0.33	0.68	0.02
40	3.46	0.92	2.48	0.25	0.46	0.32	0.68	0.02
$r_{loc} = 1.0$ bohr	U		U'		J		V	
E_{cut}^{ϵ} [Ry]	cRPA	RPA	cRPA	RPA	cRPA	RPA	cRPA	RPA
5	3.84	1.62	2.71	0.52	0.55	0.54	0.66	0.02
10	3.53	1.20	2.45	0.23	0.52	0.47	0.67	0.02
15	3.50	1.10	2.45	0.22	0.50	0.42	0.68	0.02
20	3.48	1.04	2.46	0.24	0.49	0.39	0.68	0.02
25	3.47	1.00	2.46	0.24	0.48	0.36	0.68	0.02
30	3.47	0.96	2.47	0.25	0.47	0.35	0.68	0.02
35	3.46	0.94	2.47	0.25	0.47	0.33	0.68	0.02
40	3.45	0.92	2.47	0.25	0.47	0.32	0.68	0.02
$r_{loc} = 1.5$ bohr	U		U'		J		V	
E_{cut}^{ϵ} [Ry]	cRPA	RPA	cRPA	RPA	cRPA	RPA	cRPA	RPA
5	3.80	1.59	2.62	0.44	0.57	0.56	0.66	0.02
10	3.55	1.22	2.43	0.22	0.54	0.49	0.67	0.02
15	3.54	1.13	2.45	0.24	0.51	0.43	0.68	0.02
20	3.51	1.07	2.46	0.25	0.50	0.39	0.68	0.02
25	3.50	1.01	2.46	0.25	0.49	0.37	0.68	0.02
30	3.49	0.98	2.46	0.25	0.49	0.35	0.68	0.02
35	3.48	0.95	2.46	0.25	0.48	0.34	0.68	0.02
40	3.47	0.92	2.45	0.24	0.48	0.33	0.68	0.02
$r_{loc} = 1.8$ bohr	U		U'		J		V	
E_{cut}^{ϵ} [Ry]	cRPA	RPA	cRPA	RPA	cRPA	RPA	cRPA	RPA
5	3.68	1.53	2.49	0.38	0.57	0.56	0.69	0.02
10	3.47	1.22	2.35	0.22	0.53	0.47	0.70	0.02
15	3.47	1.14	2.37	0.25	0.51	0.43	0.70	0.02
20	3.44	1.06	2.37	0.25	0.49	0.38	0.70	0.02
25	3.42	1.00	2.36	0.24	0.49	0.36	0.70	0.02
30	3.41	0.96	2.35	0.24	0.48	0.34	0.70	0.02
35	3.40	0.93	2.35	0.23	0.48	0.33	0.70	0.02
40	3.39	0.91	2.35	0.23	0.48	0.32	0.70	0.02
$r_{loc} = 2.1$ bohr	U		U'		J		V	
E_{cut}^{ϵ} [Ry]	cRPA	RPA	cRPA	RPA	cRPA	RPA	cRPA	RPA
5	3.64	1.47	2.45	0.32	0.57	0.56	0.70	0.02
10	3.50	1.21	2.38	0.24	0.53	0.47	0.71	0.02
15	3.49	1.13	2.40	0.26	0.51	0.41	0.71	0.02
20	3.46	1.04	2.38	0.25	0.49	0.37	0.71	0.02
25	3.44	0.98	2.37	0.24	0.49	0.35	0.71	0.02
30	3.43	0.94	2.37	0.23	0.49	0.33	0.71	0.02
35	3.42	0.91	2.37	0.22	0.49	0.32	0.71	0.02
40	3.42	0.90	2.36	0.23	0.48	0.31	0.71	0.02

large-scale systems. Especially, the polarization function is the bottleneck of whole calculations of the effective model derivation, and the parallelization of this part becomes important.

Fig. 17 is the acceleration rate of polarization function calculation of SrVO$_3$ by RESPACK. The calculation conditions are as follows: Wavefunction cutoff is 100 Ry, polarization-function cutoff is 20 Ry, and the total number of bands considered in the polarization function calculation is 50 band. $8 \times 8 \times 8$ k-points are sampled, and the total number of the irreducible

Table 8
Comparison of the static (ω=0) interaction parameters among the pseudopotential type, where the results based on the TM-type, ONCV-type, and RRKJ-type pseudopotentials are compared. The calculation results with the TM-type pseudopotential are obtained via xTAPP, which are denoted by TM-xTAPP, while the results with the ONCV and RRKJ pseudopotential are obtained via Quantum Espresso, which are abbreviated by ONCV-QE and RRKJ-QE, respectively. The symbol in parentheses attached to TM, i.e., (v) or (s), indicates whether the pseudopotential was made for the valence or semicore configuration, respectively. The calculation condition is as follows: $8 \times 8 \times 8$ k-point sampling, $N_{band} = 50$, $E_{cut}^{\psi} = 100$ Ry, $E_{cut}^{\epsilon} = 20$ Ry, and $\delta = 0.1$ eV. The unit of the interaction parameter is eV.

		TM(v)-xTAPP	TM(s)-xTAPP	ONCV-QE	RRKJ-QE
U	bare	15.22	15.93	15.73	15.72
	cRPA	3.46	3.50	3.50	3.19
	RPA	1.04	1.05	1.06	0.99
U'	bare	13.93	14.71	14.44	14.35
	cRPA	2.39	2.48	2.43	2.08
	RPA	0.25	0.25	0.25	0.20
J	bare	0.60	0.57	0.61	0.64
	cRPA	0.49	0.48	0.51	0.52
	RPA	0.37	0.38	0.39	0.38
V	bare	3.60	3.60	3.60	3.60
	cRPA	0.71	0.66	0.65	0.56
	RPA	0.02	0.02	0.02	0.02

Fig. 17. Acceleration performance by hybrid parallelization of RESPACK. This plot describes the acceleration rate for the polarization-function calculation for single q point of SrVO$_3$. In this figure, (n, m) next to the red dots describes the structure of the hybrid parallelization, where n is the total number for OpenMP threads and m is the total number of Message-Passing-Interface processes. About the wall time, (1,1) is 7540 s, (5,1) is 1628 s, (10,1) is 823 s, (10,2) is 458 s, (10,3) is 301 s, (10,4) is 236 s, and (10,8) is 120 s.

k-points is 35. Each computer node consists of two Intel Xeon Gold 6148 CPUs and two 100 Gbps Intel Omni-Path ports. The network topology is a full-bisection fat tree. This plot describes the acceleration rate for the polarization-function calculation for single q point. It should be noted here that this acceleration rate is for non-trivial part described in Fig. 2. As we can see from the figure, the parallelization efficiency was 80% or more with 80 cores, where the whole is 8 MPI processes and each MPI process consists of 10 OpenMP threads. This is a good performance as the non-trivial parallelization part. As mentioned in Section 3.4, RESPACK has a trivial parallelization loop for the q points in the outside of this non-trivial parallelization loop (see Fig. 3). In the present SrVO$_3$ case, the irreducible 35-q points are calculated independently in parallel. The total computational time over the 35-q point polarization calculation was about 120 s with using 2800 cores (=35 $\times$ 8 $\times$ 10 cores). This time was basically the same as that required for single q-point calculation.

Using the large-scale parallelization, RESPACK has been widely applied to *ab initio* effective-model derivation including many-body perturbation calculations of the large-scale systems. About papers on treating the large-scale systems by RESPACK, there are many reports including alkali-cluster-loaded-sodalite system (44 atoms in the unit cell) [35], alkali-doped fullerenes (63 atoms) [29], and organic compound (TMTSF)$_2$PF$_6$ (59 atoms) [71,79], κ-(BEDT-TTF)$_2$Cu(NCS)$_2$ (118 atoms) [31], and EtMe$_3$Sb[Pd(dmit)$_2$]$_2$ (228 atoms) [32]. Recently, Misawa and Yoshimi et al. performed a comprehensive study on *ab initio* derivation of effective models of organic conductors by using RESPACK [34].

7. Conclusion

In conclusion, we present a new software RESPACK for deriving effective low-energy models of materials from first principles. The software contains programs for computing maximally-localized Wannier functions, RPA response functions, and matrix elements for screened interaction with respect to the Wannier functions. RESPACK is freely available under the GNU General Public Licence [80]. RESPACK is written in Fortran90 and supports plane-wave DFT codes xTAPP [81] and Quantum Espresso [62,63], for which an interface script that converts the band-calculation results to the RESPACK inputs is provided. As an

important notice, RESPACK currently supports *ab initio* codes with the norm-conserving pseudopotential. The present paper focuses on the derivation of the effective model, but it has currently been extended to the GW calculation, effective-model derivation with spin–orbit interaction, and electron–lattice coupling evaluation. We will report on these additional features in near future.

Declaration of competing interest

The authors declare that they have no known competing financial interests or personal relationships that could have appeared to influence the work reported in this paper.

Table A.9

Namelists available in an input file (`input.in`) of RESPACK. The second column gives an executable file to which each namelist relates. The third column is a brief explanation of each namelist.

Namelist	Executable file	Explanation
&param_wannier	calc_wannier	Wannier-function calculation
&param_interpolation	calc_wannier	Wannier-interpolated band calculation
&param_visualization	calc_wannier	Visualization of Wannier function
&param_chiqw	calc_chiqw	Polarization and dielectric calculations
&param_calc_int	calc_w3d	Direct-Coulomb integral calculation
&param_calc_int	calc_j3d	Exchange integral calculation

Appendix A. Input files

In this appendix, we describe details of the input file `input.in` for specifying the calculation condition of RESPACK. The `input.in` is given in the FORTRAN namelist format. Table A.9 lists six namelists available in `input.in`. The namelist &param_wannier contains variables for the Wannier-function calculation. The namelists &param_interpolation and &param_visualization describe variables for the Wannier-interpolation band and the visualization of the realspace Wannier functions, respectively. These three namelists are read by a common executable file `calc_wannier`. This executable file is generated by compilation of source code in the directory RESPACK/src/wannier. The namelist &param_chiqw contains parameters for calculations of polarization and dielectric functions and is read by an executable file `calc_chiqw` which is created by compilation of source code in RESPACK/src/chiqw. The namelist &param_calc_int describes variables for direct-Coulomb and exchange-integral calculation and is read by executable files `calc_w3d` and `calc_j3d`. These are made by compilation in the source code in RESPACK/src/calc_int.

A.1. &param_wannier

Table A.10 shows main four variables in the namelist &param_wannier. N_wannier is the total number of the Wannier function to be calculated. Lower_energy_window and Upper_energy_window specify the energy window and the Bloch bands in the energy window are used for the Wannier-function calculation. The user has to set proper values by seeing the band dispersion obtained with DFT band calculations. N_initial_guess is the number of initial Gaussian for the Wannier-function calculation. The user must enter initial-guess information just below this namelist (see Table 1). vec_ini(1:N_initial_guess) in Table A.10 are variables to specify the initial guess and is treated as *type* in FORTRAN. vec_ini(i)%orb specifies the orbital type of the ith initial guess, where %orb can take a character of s, px, py, pz, dxy, dyz, dzx, dx2, dz2. The initial guess is treated with the Gaussian function, $\exp(-\alpha_i|\mathbf{r} - \mathbf{R}_i|^2)$, where α_i=%a is orbital exponent of the ith Gaussian. The Gaussian position $\mathbf{R}_i = x\mathbf{a}_1 + y\mathbf{a}_2 + z\mathbf{a}_3$ with x=%x, y=%y, and z=%z are given in the fractional coordinates, where $\mathbf{a}_1$, $\mathbf{a}_2$, and $\mathbf{a}_3$ are the lattice vectors in the calculation cell. Note that one has to enter N_initial_guess pieces of the vec_init information. Specific descriptions are given in Table 1.

A.2. &param_interpolation

Tables A.11 summarizes main variables in the namelist &param_interpolation to draw the Wannier-interpolated band. The user specifies the total number of symmetric k points in the dispersion line as N_sym_points, and, just below this

Table A.10

Main variables in namelist &param_wannier to construct maximally-localized Wannier functions. The variable type and its brief explanation are shown in the second and third columns, respectively. The lower five variables in vec_ini are information about initial guesses. Note that vec_ini is treated as *type* of FORTRAN. The initial guess is specified by the orbital type "s, px, py, pz, dxy, dyz, dzx, dx2, dz2") and parameters in the Gaussian function, $\exp(-\alpha_i|\mathbf{r} - \mathbf{R}_i|^2)$. Here, α_i is an orbital exponent of the ith Gaussian, and $\mathbf{R}_i = x\mathbf{a}_1 + y\mathbf{a}_2 + z\mathbf{a}_3$ is the Gaussian position in the fractional coordinates, where $\mathbf{a}_1$, $\mathbf{a}_2$, and $\mathbf{a}_3$ are the lattice vectors in the calculation cell.

Namelist &param_wannier

Variable	Type	Explanation
N_wannier	Integer	Number of the Wannier functions
Lower_energy_window	Real	Lower limit of energy window in eV
Upper_energy_window	Real	Upper limit of energy window in eV
N_initial_guess	Integer	Number of initial Gaussians
vec_ini(i)%orb	Character	Orbital type of ith Gaussian
vec_ini(i)%a	Real	Orbital exponent of ith Gaussian
vec_ini(i)%x	Real	x component of ith Gaussian position
vec_ini(i)%y	Real	y component of ith Gaussian position
vec_ini(i)%z	Real	z component of ith Gaussian position

Table A.11

Main variables in namelist &param_interpolation to draw the Wannier-interpolated band. The type and brief explanation of the variable are shown in the second and third columns, respectively. Lower three variables specify the symmetric k points $\{\mathbf{k}_i\}$ in the dispersion line. These $\{\mathbf{k}_i\}$ information are treated as *array* SK_sym_pts(1:3,1:N_sym_points) in FORTRAN, where $\mathbf{k}_i = s_1\mathbf{b}_1 + s_2\mathbf{b}_2 + s_3\mathbf{b}_3$ is the ith symmetric k point with $\mathbf{b}_1$, $\mathbf{b}_2$, and $\mathbf{b}_3$ being the basic reciprocal lattice vectors.

Namelist &param_interpolation

Variable	Type	Explanation
N_sym_points	Integer	Number of symmetric k points
SK_sym_pts(1,i)	Real	$s1$ component of ith symmetric k point
SK_sym_pts(2,i)	Real	$s2$ component of ith symmetric k point
SK_sym_pts(3,i)	Real	$s3$ component of ith symmetric k point

Table A.12

Main parameter in namelist &param_visualization to calculate realspace Wannier functions. When the variable Flg_vis_wannier is set to 1, RESPACK calculates the visualization data of the Wannier function. Outputs can be drawn by software VESTA [67].

Namelist &param_visualization

Variable	Type	Explanation
Flg_vis_wannier	Integer	Visualization of Wannier function (do not: 0, do: 1)

namelist, describes the coordinates $\{(s_1, s_2, s_3)\}$ of the symmetric k vectors (see Table 1 for concrete descriptions). Here, $\mathbf{k}_i = s_1\mathbf{b}_1 + s_2\mathbf{b}_2 + s_3\mathbf{b}_3$ with $\mathbf{b}_1$, $\mathbf{b}_2$, and $\mathbf{b}_3$ being the basic reciprocal lattice vectors. These variables are read as *array* SK_sym_pts (1:3,1:N_sym_points). Usually, the same k points as those employed in the DFT band calculation are adopted.

A.3. &param_visualization

We show in Table A.12 parameters in the namelist &param_visualization. By default, RESPACK skips the visualization calculation of the realspace Wannier function. So, the user must set Flg_vis_wannier to 1 when calculating visualization data. Structural data of the same spatial range as the Wannier-function data is also output as cif (Crystallographic Information File) format. All the results can be drawn by software VESTA [67].

A.4. &param_chiqw

Next, we list in Table A.13 main parameters of the namelist &param_chiqw. In this namelist, the user specifies the calculation

Table A.13

Main variables in namelist `&param_chiqw` to calculate polarization and dielectric functions. The variable type and its brief explanation are shown in the second and third columns, respectively. See the text for more detailed explanation of each variable.

Namelist `&param_chiqw`		
Variable	Type	Explanation
`Ecut_for_eps`	Real	Cutoff energy for polarization in Rydberg
`Num_freq_grid`	Integer	Number of frequency grid
`Green_func_delt`	Real	Smearing value in eV
`MPI_num_qcomm`	Integer	Degree of parallelism for q-point calculation
`MPI_num_proc_per_qcomm`	Integer	Number of MPI processes per q-community
`Flg_cRPA`	Integer	Constrained RPA (do not: 0, do: 1)

Table A.14

Main parameter in namelist `&param_calc_int` to evaluate the direct-Coulomb and exchange integrals. A common namelist is used for the direct-Coulomb and exchange calculations. The variable `Calc_ifreq` specifies the frequency number of the output interaction integrals, and by default, the $\omega = 0$ results are output (`Calc_ifreq=1`).

Namelist `&param_calc_int`		
Variable	Type	Explanation
`Calc_ifreq`	Integer	Frequency number of output interaction matrix

condition of the polarization and dielectric functions. `Ecut_for_eps` is the cutoff energy for the polarization function. Default value is set to 1/10 of wave-function cutoff E_{cut}^{ψ}. `Num_freq_grid` is the total number of the frequency grid. By default, a log grid of 70 points is generated. The maximum excitation energy E_{max} is estimated from the total bands considered in the polarization function, and the range of the frequency grid is set to $3E_{max}$ to consider the Lorentz tail of the polarization function. See Section 3.2 for details. `Green_func_delt` is smearing value used in the generalized tetrahedron calculation (0.1 eV by default). In RESPACK, the polarization calculation is performed in parallel. To this end, two variables `MPI_num_qcomm` and `MPI_num_proc_per_qcomm` are prepared. `MPI_num_qcomm` is a variable for parallel computation on the q points and defines the number of q-community. `MPI_num_proc_per_qcomm` specifies the total number of MPI processes in each q-community. Note that when `mod(N_MPI,MPI_num_qcomm)/=0`, the *chiqw* program stops, where `N_MPI` is the total number of the MPI processes and this value is set in the job script. By default, `MPI_num_qcomm=1` and `MPI_num_proc_per_qcomm=N_MPI`. Details of the parallel calculation can be found in Section 3.4. Lastly, `Flg_cRPA` is a variable to specify the constrained RPA calculation. In the default setting, `Flg_cRPA=0` and the program performs a usual RPA calculation.

A.5. `&param_calc_int`

Table A.14 gives a main variable in the namelist `&param_calc_int`. Evaluations of the direct-Coulomb and exchange integrals are executed in separate executable files (the direct-Coulomb integral for `calc_w3d` and the exchange integral for `calc_j3d`), but these calculations are performed with the common namelist `&param_calc_int`. RESPACK calculates the frequency-dependent effective interaction but its data size is huge. So, the user can set an output frequency number of the effective interaction matrix as `Calc_ifreq`. By default, the results of $\omega = 0$ are output (`Calc_ifreq=1`).

Appendix B. Transfer analysis

When the RESPACK job (*wannier*, *chiqw*, *calc_w3d*, *calc_j3d*) is completed, a directory `dir-model` is created under the calculation directory, and the following 9 files are generated in `dir-model`:

1. `zvo_hr.dat` (transfer integrals)
2. `zvo_dr.dat` (density matrix)
3. `zvo_ur.dat` (direct Coulomb integrals)
4. `zvo_jr.dat` (exchange integrals)
5. `zvo_geom.dat` (Wannier centers: text format)
6. `zvo_geom.xsf` (Wannier centers: xsf format)
7. `zvo_bandkpts.dat` [k-grid in Eq. (52)(a)]
8. `zvo_mkkpts.dat` [k-grid in Eq. (52)(b)]
9. `zvo_ef.dat` (Fermi energy)

These `zvo` files are used for the connection to model-solver software mVMC [82] and $\mathcal{H}\Phi$ [83]. The `zvo_hr.dat`, `zvo_dr.dat`, `zvo_ur.dat`, and `zvo_jr.dat` are output in the WANNIER90 format [84]. From these `zvo` files, the interface code provided from mVMC and $\mathcal{H}\Phi$ generate the input files of mVMC and $\mathcal{H}\Phi$ automatically. Thus, the user can easily make the inputs for the post-RESPACK calculations. Refer to the manual sites of mVMC and $\mathcal{H}\Phi$ for the interface program and usage.

RESPACK provides a utility tool to analyze transfer data, and the above 9 files are also used for this purpose. Using a PYTHON script `tr.py` in the directory `RESPACK/util/transfer_analysis` and an executable file `calc_tr` by compiling source code in the directory `RESPACK/src/transfer_analysis`, one can execute the transfer analysis. Preparation for the calculations so far is as follows:

```
> cd RESPACK/src/transfer_analysis
> make
> cp calc_tr calculation_directory/.
> cd RESPACK/util/transfer_analysis
> cp tr.py calculation_directory/.
```

Fig. B.18 is a flow diagram of the transfer analysis. With the data files in `dir-model`, the executable file `calc_tr`, and the PYTHON script `tr.py`, the transfer analysis is performed.

This `tr.py` code is basically a sorting code for the transfer data. The user can classify and sort the transfer data with the same absolute value. Besides the sorting function, the band-dispersion calculation, the density-of-states calculation, and the Fermi-surface calculation, etc. can be executed. Table B.15 summarizes the command lines available in `tr.py`. With this program, the user can change the calculation condition such as energy threshold (`--ecut`) and spatial range (`--rcut`) of transfers, and k-grid size (`--kgrd`) considered in the band-dispersion and density-of-states calculations.

Fig. B.19 is examples of the transfer analysis for SrVO$_3$. The panel (a) and (b) show the energy-cutoff dependence of the Wannier-interpolated band and density of states, respectively. These results were obtained by performing the following commands

- Band-dispersion calculation [Fig. B.19(a)]:
  ```
  > python tr.py --bnd --ecut=E
  ```
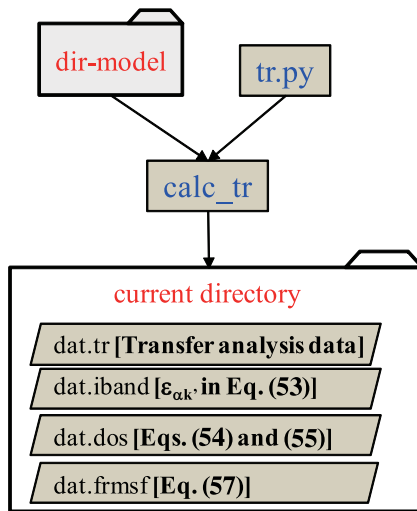
Fig. B.18. Flow diagram of transfer analysis. With the data in dir-model, an executable file calc_tr, a PYTHON script tr.py, the transfer analysis is performed. Note that tr.py calls the executable file calc_tr internally. Calculation results are output in the current directory.
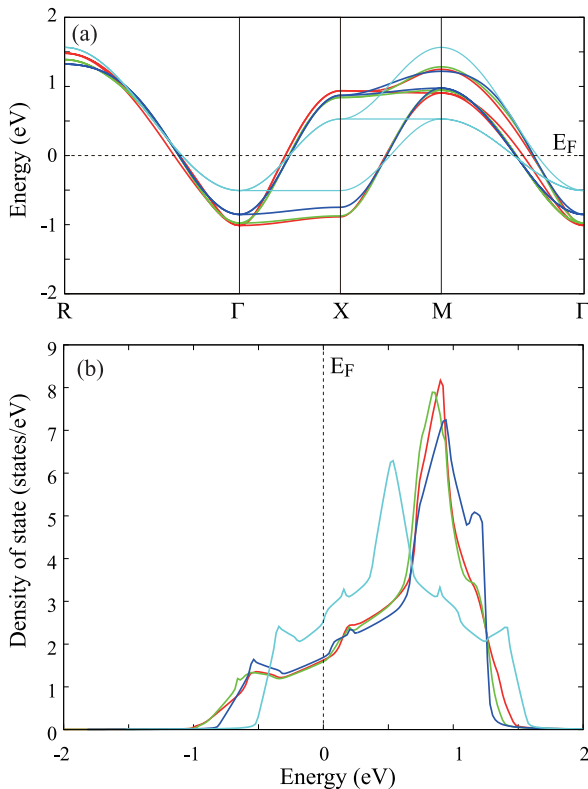
Fig. B.19. Dependence of the t_{2g}-band properties of $SrVO_3$ on energy cutoff of transfer integrals: (a) The Wannier-interpolated band: python tr.py --bnd --ecut=0.00 (red), 0.01 (green), 0.05 (blue), 0.10 (right blue). (b) Density of states: python tr.py --dos --ecut=0.00 (red), 0.01 (green), 0.05 (blue), 0.10 (right blue). The Fermi energy is zero. (For interpretation of the references to color in this figure legend, the reader is referred to the web version of this article.)

- Density-of-states calculation [Fig. B.19(b)]:

  > python tr.py --dos --ecut=E

with E being a value of the energy threshold in unit of eV. In the figures, we show the results of $E = 0.00$ (red), 0.01 (green), 0.05 (blue), 0.1 (right-blue) eV. With --ecut=0.1, only
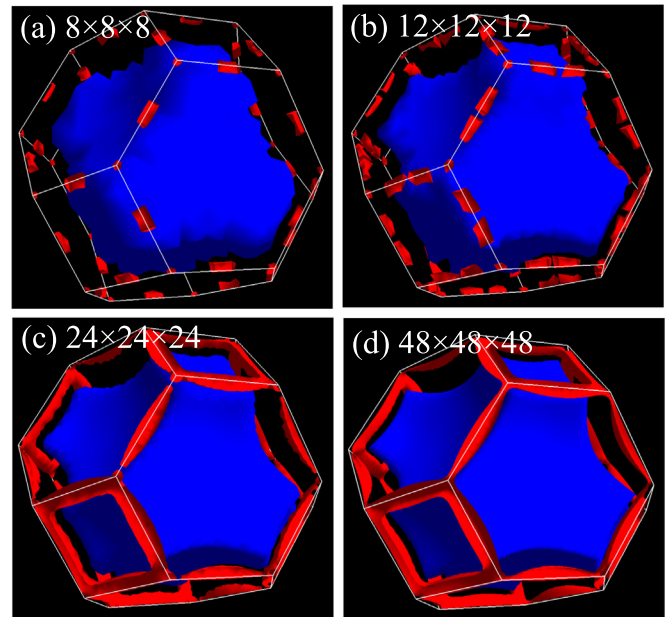
Fig. B.20. Dependence of the Fermi surface of Al on the k-grid density (drawn by FERMISURFER [60,85]): python tr.py --frm --kgrd='8 8 8' (a), '12 12 12' (b), '24 24 24' (c), '48 48 48' (d).

Table B.15
Command line options available in the PYTHON script tr.py in Fig. B.18. A brief explanation is given in the right column. The part written in bold font indicates the default setting. See the text for the usage of tr.py.

Command	Explanation
-h	Display argument list
--bnd	Wannier-interpolated band calculation
--dos	Density of state (DOS) calculation
--frm	Fermi-surface data generation for Fermisurfer
--diff D	Threshold for detecting equivalent transfers (**0.01 eV**)
--ecut E	Cut transfers below E (**0.00 eV**)
--rcut R	Cut transfers over R (**100 Å**)
--elec N	Set electron numbers in unit cell to N (**no setting**)
--delta δ	Set broadening for DOS calculation to δ (**0.01 eV**)
--kgrd='n m l'	Set k-grid to $n \times m \times l$ (**the same as the band calculation**)

the nearest neighbor transfers are considered in the calculations (see Fig. 8), and therefore the band dispersion and density of states are appreciably changed from others.

As another example, we show in Fig. B.20 the k-grid density dependence of the Fermi surface. This is an Al result. Accurate description for a small Fermi surface colored by red needs dense k-grid density. The calculation is performed as

> > python tr.py --frm --kgrd='n m l'

with n, m, and l being numbers of k-grid along the basic reciprocal lattice vectors $\mathbf{b}_1$, $\mathbf{b}_2$, and $\mathbf{b}_3$, respectively.

References

[1] P. Hohenberg, W. Kohn, Phys. Rev. 136 (1964) B864–B871, http://dx.doi.org/10.1103/PhysRev.136.B864, https://link.aps.org/doi/10.1103/PhysRev.136.B864.

[2] W. Kohn, L.J. Sham, Phys. Rev. 140 (1965) A1133–A1138, http://dx.doi.org/10.1103/PhysRev.140.A1133, https://link.aps.org/doi/10.1103/PhysRev.140.A1133.

[3] J.-I. Iwata, D. Takahashi, A. Oshiyama, T. Boku, K. Shiraishi, S. Okada, K. Yabana, J. Comput. Phys. 229 (6) (2010) 2339–2363,

http://dx.doi.org/10.1016/j.jcp.2009.11.038, http://www.sciencedirect.com/science/article/pii/S0021999109006676.

[4] N. Hine, P. Haynes, A. Mostofi, C.-K. Skylaris, M. Payne, Comput. Phys. Comm. 180 (7) (2009) 1041–1053, http://dx.doi.org/10.1016/j.cpc.2008.12.023, http://www.sciencedirect.com/science/article/pii/S0010465508004414.

[5] T.V.T. Duy, T. Ozaki, Comput. Phys. Comm. 185 (1) (2014) 153–164, http://dx.doi.org/10.1016/j.cpc.2013.08.028, http://www.sciencedirect.com/science/article/pii/S0010465513003020.

[6] T.V.T. Duy, T. Ozaki, Comput. Phys. Comm. 185 (3) (2014) 777–789, http://dx.doi.org/10.1016/j.cpc.2013.11.008, http://www.sciencedirect.com/science/article/pii/S0010465513004013.

[7] D.R. Bowler, R. Choudhury, M.J. Gillan, T. Miyazaki, Phys. Status Solidi b 243 (5) (2006) 989–1000, http://dx.doi.org/10.1002/pssb.200541386, https://onlinelibrary.wiley.com/doi/abs/10.1002/pssb.200541386 arXiv:https://onlinelibrary.wiley.com/doi/pdf/10.1002/pssb.200541386.

[8] Qbox Web page [online, cited http://qboxcode.org/].

[9] A. van de Walle, M. Asta, G. Ceder, CALPHAD 26 (4) (2002) 539–553, http://dx.doi.org/10.1016/S0364-5916(02)80006-2, http://www.sciencedirect.com/science/article/pii/S0364591602800062.

[10] W. Zhang, A.R. Oganov, A.F. Goncharov, Q. Zhu, S.E. Boulfelfel, A.O. Lyakhov, E. Stavrou, M. Somayazulu, V.B. Prakapenka, Z. Konôpková, Science 342 (6165) (2013) 1502–1505, http://dx.doi.org/10.1126/science.1244989, arXiv:https://science.sciencemag.org/content/342/6165/1502.full.pdf https://science.sciencemag.org/content/342/6165/1502.

[11] M. Imada, T. Miyake, J. Phys. Soc. Japan 79 (11) (2010) 112001, http://dx.doi.org/10.1143/JPSJ.79.112001.

[12] F. Aryasetiawan, M. Imada, A. Georges, G. Kotliar, S. Biermann, A.I. Lichtenstein, Phys. Rev. B 70 (2004) 195104, http://dx.doi.org/10.1103/PhysRevB.70.195104, https://link.aps.org/doi/10.1103/PhysRevB.70.195104.

[13] M. Kawamura, K. Yoshimi, T. Misawa, Y. Yamaji, S. Todo, N. Kawashima, Comput. Phys. Comm. 217 (2017) 180–192, http://dx.doi.org/10.1016/j.cpc.2017.04.006, http://www.sciencedirect.com/science/article/pii/S0010465517301200.

[14] A. Georges, G. Kotliar, W. Krauth, M.J. Rozenberg, Rev. Modern Phys. 68 (1996) 13–125, http://dx.doi.org/10.1103/RevModPhys.68.13, https://link.aps.org/doi/10.1103/RevModPhys.68.13.

[15] G. Kotliar, S.Y. Savrasov, K. Haule, V.S. Oudovenko, O. Parcollet, C.A. Marianetti, Rev. Modern Phys. 78 (2006) 865–951, http://dx.doi.org/10.1103/RevModPhys.78.865, https://link.aps.org/doi/10.1103/RevModPhys.78.865.

[16] D. Tahara, M. Imada, J. Phys. Soc. Japan 77 (9) (2008) 093703, http://dx.doi.org/10.1143/JPSJ.77.093703.

[17] D. Tahara, M. Imada, J. Phys. Soc. Japan 77 (11) (2008) 114701, http://dx.doi.org/10.1143/JPSJ.77.114701.

[18] T. Misawa, S. Morita, K. Yoshimi, M. Kawamura, Y. Motoyama, K. Ido, T. Ohgoe, M. Imada, T. Kato, Comput. Phys. Comm. 235 (2019) 447–462, http://dx.doi.org/10.1016/j.cpc.2018.08.014, http://www.sciencedirect.com/science/article/pii/S0010465518303102.

[19] K. Nakamura, Y. Yoshimoto, R. Arita, S. Tsuneyuki, M. Imada, Phys. Rev. B 77 (2008) 195126, http://dx.doi.org/10.1103/PhysRevB.77.195126, https://link.aps.org/doi/10.1103/PhysRevB.77.195126.

[20] K. Nakamura, R. Arita, M. Imada, J. Phys. Soc. Japan 77 (9) (2008) 093711, http://dx.doi.org/10.1143/JPSJ.77.093711.

[21] T. Miyake, K. Nakamura, R. Arita, M. Imada, J. Phys. Soc. Japan 79 (4) (2010) 044705, http://dx.doi.org/10.1143/JPSJ.79.044705.

[22] T. Misawa, K. Nakamura, M. Imada, J. Phys. Soc. Japan 80 (2) (2011) 023704, http://dx.doi.org/10.1143/JPSJ.80.023704.

[23] M. Hirayama, Y. Yamaji, T. Misawa, M. Imada, Phys. Rev. B 98 (2018) 134501, http://dx.doi.org/10.1103/PhysRevB.98.134501, https://link.aps.org/doi/10.1103/PhysRevB.98.134501.

[24] M. Hirayama, T. Misawa, T. Ohgoe, Y. Yamaji, M. Imada, Phys. Rev. B 99 (2019) 245155, http://dx.doi.org/10.1103/PhysRevB.99.245155, https://link.aps.org/doi/10.1103/PhysRevB.99.245155.

[25] Y. Nomura, M. Hirayama, T. Tadano, Y. Yoshimoto, K. Nakamura, R. Arita, Phys. Rev. B 100 (2019) 205138, http://dx.doi.org/10.1103/PhysRevB.100.205138, https://link.aps.org/doi/10.1103/PhysRevB.100.205138.

[26] M. Hirayama, T. Tadano, Y. Nomura, R. Arita, Phys. Rev. B 101 (2020) 075107, http://dx.doi.org/10.1103/PhysRevB.101.075107, https://link.aps.org/doi/10.1103/PhysRevB.101.075107.

[27] L. Vaugier, H. Jiang, S. Biermann, Phys. Rev. B 86 (2012) 165105, http://dx.doi.org/10.1103/PhysRevB.86.165105, https://link.aps.org/doi/10.1103/PhysRevB.86.165105.

[28] T.O. Wehling, E. Şaşıoğlu, C. Friedrich, A.I. Lichtenstein, M.I. Katsnelson, S. Blügel, Phys. Rev. Lett. 106 (2011) 236805, http://dx.doi.org/10.1103/PhysRevLett.106.236805, https://link.aps.org/doi/10.1103/PhysRevLett.106.236805.

[29] Y. Nomura, K. Nakamura, R. Arita, Phys. Rev. B 85 (2012) 155452, http://dx.doi.org/10.1103/PhysRevB.85.155452, https://link.aps.org/doi/10.1103/PhysRevB.85.155452.

[30] M. Kim, Y. Nomura, M. Ferrero, P. Seth, O. Parcollet, A. Georges, Phys. Rev. B 94 (2016) 155152, http://dx.doi.org/10.1103/PhysRevB.94.155152, https://link.aps.org/doi/10.1103/PhysRevB.94.155152.

[31] K. Nakamura, Y. Yoshimoto, T. Kosugi, R. Arita, M. Imada, J. Phys. Soc. Japan 78 (8) (2009) 083710, http://dx.doi.org/10.1143/JPSJ.78.083710.

[32] K. Nakamura, Y. Yoshimoto, M. Imada, Phys. Rev. B 86 (2012) 205117, http://dx.doi.org/10.1103/PhysRevB.86.205117, https://link.aps.org/doi/10.1103/PhysRevB.86.205117.

[33] H. Shinaoka, T. Misawa, K. Nakamura, M. Imada, J. Phys. Soc. Japan 81 (3) (2012) 034701, http://dx.doi.org/10.1143/JPSJ.81.034701.

[34] T. Misawa, K. Yoshimi, T. Tsumuraya, Phys. Rev. Res. 2 (2020) 032072, http://dx.doi.org/10.1103/PhysRevResearch.2.032072, https://link.aps.org/doi/10.1103/PhysRevResearch.2.032072.

[35] K. Nakamura, T. Koretsune, R. Arita, Phys. Rev. B 80 (2009) 174420, http://dx.doi.org/10.1103/PhysRevB.80.174420, https://link.aps.org/doi/10.1103/PhysRevB.80.174420.

[36] Y. Nohara, K. Nakamura, R. Arita, J. Phys. Soc. Japan 80 (12) (2011) 124705, http://dx.doi.org/10.1143/JPSJ.80.124705.

[37] E. Şaşıoğlu, C. Friedrich, S. Blügel, Phys. Rev. Lett. 109 (2012) 146401, http://dx.doi.org/10.1103/PhysRevLett.109.146401, https://link.aps.org/doi/10.1103/PhysRevLett.109.146401.

[38] P. Hansmann, L. Vaugier, H. Jiang, S. Biermann, J. Phys.: Condens. Matter 25 (9) (2013) 094005, http://dx.doi.org/10.1088/0953-8984/25/9/094005.

[39] S. Okamoto, W. Zhu, Y. Nomura, R. Arita, D. Xiao, N. Nagaosa, Phys. Rev. B 89 (2014) 195121, http://dx.doi.org/10.1103/PhysRevB.89.195121, https://link.aps.org/doi/10.1103/PhysRevB.89.195121.

[40] T. Tadano, Y. Nomura, M. Imada, Phys. Rev. B 99 (2019) 155148, http://dx.doi.org/10.1103/PhysRevB.99.155148, https://link.aps.org/doi/10.1103/PhysRevB.99.155148.

[41] R. Arita, J. Kuneš, A.V. Kozhevnikov, A.G. Eguiluz, M. Imada, Phys. Rev. Lett. 108 (2012) 086403, http://dx.doi.org/10.1103/PhysRevLett.108.086403.

[42] Y. Yamaji, Y. Nomura, M. Kurita, R. Arita, M. Imada, Phys. Rev. Lett. 113 (2014) 107201, http://dx.doi.org/10.1103/PhysRevLett.113.107201, https://link.aps.org/doi/10.1103/PhysRevLett.113.107201.

[43] F. Nilsson, R. Sakuma, F. Aryasetiawan, Phys. Rev. B 88 (2013) 125123, http://dx.doi.org/10.1103/PhysRevB.88.125123, https://link.aps.org/doi/10.1103/PhysRevB.88.125123.

[44] J.-B. Morée, B. Amadon, Phys. Rev. B 98 (2018) 205101, http://dx.doi.org/10.1103/PhysRevB.98.205101, https://link.aps.org/doi/10.1103/PhysRevB.98.205101.

[45] B. Amadon, T. Applencourt, F. Bruneval, Phys. Rev. B 89 (2014) 125110, http://dx.doi.org/10.1103/PhysRevB.89.125110, https://link.aps.org/doi/10.1103/PhysRevB.89.125110.

[46] P. Seth, P. Hansmann, A. van Roekeghem, L. Vaugier, S. Biermann, Phys. Rev. Lett. 119 (2017) 056401, http://dx.doi.org/10.1103/PhysRevLett.119.056401, https://link.aps.org/doi/10.1103/PhysRevLett.119.056401.

[47] T. Miyake, F. Aryasetiawan, M. Imada, Phys. Rev. B 80 (2009) 155134, http://dx.doi.org/10.1103/PhysRevB.80.155134, https://link.aps.org/doi/10.1103/PhysRevB.80.155134.

[48] E. Şaşıoğlu, C. Friedrich, S. Blügel, Phys. Rev. B 83 (2011) 121101, http://dx.doi.org/10.1103/PhysRevB.83.121101, https://link.aps.org/doi/10.1103/PhysRevB.83.121101.

[49] K. Nakamura, Y. Yoshimoto, Y. Nohara, M. Imada, J. Phys. Soc. Japan 79 (12) (2010) 123708, http://dx.doi.org/10.1143/JPSJ.79.123708.

[50] Y. Nomura, M. Kaltak, K. Nakamura, C. Taranto, S. Sakai, A. Toschi, R. Arita, K. Held, G. Kresse, M. Imada, Phys. Rev. B 86 (2012) 085117, http://dx.doi.org/10.1103/PhysRevB.86.085117, https://link.aps.org/doi/10.1103/PhysRevB.86.085117.

[51] RESPACK Web page [online, cited https://sites.google.com/view/kazuma7k6r].

[52] N. Marzari, D. Vanderbilt, Phys. Rev. B 56 (1997) 12847–12865, http://dx.doi.org/10.1103/PhysRevB.56.12847, https://link.aps.org/doi/10.1103/PhysRevB.56.12847.

[53] I. Souza, N. Marzari, D. Vanderbilt, Phys. Rev. B 65 (2001) 035109, http://dx.doi.org/10.1103/PhysRevB.65.035109, https://link.aps.org/doi/10.1103/PhysRevB.65.035109.

[54] T. Fujiwara, S. Yamamoto, Y. Ishii, J. Phys. Soc. Japan 72 (4) (2003) 777–780, http://dx.doi.org/10.1143/JPSJ.72.777.

[55] Y. Nohara, S. Yamamoto, T. Fujiwara, Phys. Rev. B 79 (2009) 195110, http://dx.doi.org/10.1103/PhysRevB.79.195110, https://link.aps.org/doi/10.1103/PhysRevB.79.195110.

[56] M.S. Hybertsen, S.G. Louie, Phys. Rev. B 35 (1987) 5585–5601, http://dx.doi.org/10.1103/PhysRevB.35.5585, https://link.aps.org/doi/10.1103/PhysRevB.35.5585.

[57] C. Ambrosch-Draxl, J.O. Sofo, Comput. Phys. Comm. 175 (1) (2006) 1–14, http://dx.doi.org/10.1016/j.cpc.2006.03.005, http://www.sciencedirect.com/science/article/pii/S0010465506001299.

[58] A. Marini, G. Onida, R. Del Sole, Phys. Rev. B 64 (2001) 195125, http://dx.doi.org/10.1103/PhysRevB.64.195125, https://link.aps.org/doi/10.1103/PhysRevB.64.195125.

[59] M.S. Hybertsen, S.G. Louie, Phys. Rev. B 34 (1986) 5390–5413, http://dx.doi.org/10.1103/PhysRevB.34.5390, https://link.aps.org/doi/10.1103/PhysRevB.34.5390.

[60] FermiSurfer Web page [online, cited http://fermisurfer.osdn.jp/].

[61] J. Yamauchi, M. Tsukada, S. Watanabe, O. Sugino, Phys. Rev. B 54 (1996) 5586–5603, http://dx.doi.org/10.1103/PhysRevB.54.5586, https://link.aps.org/doi/10.1103/PhysRevB.54.5586.

[62] P. Giannozzi, S. Baroni, N. Bonini, M. Calandra, R. Car, C. Cavazzoni, D. Ceresoli, G.L. Chiarotti, M. Cococcioni, I. Dabo, A. Dal Corso, S. de Gironcoli, S. Fabris, G. Fratesi, R. Gebauer, U. Gerstmann, C. Gougoussis, A. Kokalj, M. Lazzeri, L. Martin-Samos, N. Marzari, F. Mauri, R. Mazzarello, S. Paolini, A. Pasquarello, L. Paulatto, C. Sbraccia, S. Scandolo, G. Sclauzero, A.P. Seitsonen, A. Smogunov, P. Umari, R.M. Wentzcovitch, J. Phys.: Condens. Matter 21 (39) (2009) 395502, http://www.quantum-espresso.org (19pp).

[63] P. Giannozzi, O. Andreussi, T. Brumme, O. Bunau, M.B. Nardelli, M. Calandra, R. Car, C. Cavazzoni, D. Ceresoli, M. Cococcioni, N. Colonna, I. Carnimeo, A.D. Corso, S. de Gironcoli, P. Delugas, R.A.D. Jr, A. Ferretti, A. Floris, G. Fratesi, G. Fugallo, R. Gebauer, U. Gerstmann, F. Giustino, T. Gorni, J. Jia, M. Kawamura, H.-Y. Ko, A. Kokalj, E. Küçükbenli, M. Lazzeri, M. Marsili, N. Marzari, F. Mauri, N.L. Nguyen, H.-V. Nguyen, A.O. de-la Roza, L. Paulatto, S. Poncé, D. Rocca, R. Sabatini, B. Santra, M. Schlipf, A.P. Seitsonen, A. Smogunov, I. Timrov, T. Thonhauser, P. Umari, N. Vast, X. Wu, S. Baroni, J. Phys.: Condens. Matter 29 (46) (2017) 465901.

[64] L. Kleinman, D.M. Bylander, Phys. Rev. Lett. 48 (1982) 1425–1428, http://dx.doi.org/10.1103/PhysRevLett.48.1425, https://link.aps.org/doi/10.1103/PhysRevLett.48.1425.

[65] N. Troullier, J.L. Martins, Phys. Rev. B 43 (1991) 1993–2006, http://dx.doi.org/10.1103/PhysRevB.43.1993, https://link.aps.org/doi/10.1103/PhysRevB.43.1993.

[66] J.P. Perdew, K. Burke, M. Ernzerhof, Phys. Rev. Lett. 77 (1996) 3865–3868, http://dx.doi.org/10.1103/PhysRevLett.77.3865, https://link.aps.org/doi/10.1103/PhysRevLett.77.3865.

[67] K. Momma, F. Izumi, J. Appl. Crystallogr. 44 (2011) 1272, http://dx.doi.org/10.1107/S0021889811038970.

[68] In this calculation, since the broadening factor δ is introduced, the real part of the macroscopic dielectric function does not actually diverge and takes a value $\sim -\omega_{pl}^2/\delta^2$ at the $\omega \to 0$ limit [57].

[69] We have implemented this correction for xTAPP to check the fact that the effect of non-local correction on the optical spectrum is small in SrVO$_3$. This correction is supported for xTAPP, but it is not yet supported for Quantum Espresso.

[70] J.R. Yates, X. Wang, D. Vanderbilt, I. Souza, Phys. Rev. B 75 (2007) 195121, http://dx.doi.org/10.1103/PhysRevB.75.195121, https://link.aps.org/doi/10.1103/PhysRevB.75.195121.

[71] K. Nakamura, Y. Nohara, Y. Yosimoto, Y. Nomura, Phys. Rev. B 93 (2016) 085124, http://dx.doi.org/10.1103/PhysRevB.93.085124, https://link.aps.org/doi/10.1103/PhysRevB.93.085124.

[72] H. Makino, I.H. Inoue, M.J. Rozenberg, I. Hase, Y. Aiura, S. Onari, Phys. Rev. B 58 (1998) 4384–4393, http://dx.doi.org/10.1103/PhysRevB.58.4384, https://link.aps.org/doi/10.1103/PhysRevB.58.4384.

[73] S. Domenech, H.P. Martins, E.B. Guedes, R.J. Ochekoski Mossanek, M. Abbate, Eur. Phys. J. B 92 (8) (2019) 169, http://dx.doi.org/10.1140/epjb/e2019-100187-3.

[74] P. Wissgott, J. Kuneš, A. Toschi, K. Held, Phys. Rev. B 85 (2012) 205133, http://dx.doi.org/10.1103/PhysRevB.85.205133, https://link.aps.org/doi/10.1103/PhysRevB.85.205133.

[75] D.R. Hamann, Phys. Rev. B 88 (2013) 085117, http://dx.doi.org/10.1103/PhysRevB.88.085117, https://link.aps.org/doi/10.1103/PhysRevB.88.085117.

[76] A.M. Rappe, K.M. Rabe, E. Kaxiras, J.D. Joannopoulos, Phys. Rev. B 41 (1990) 1227–1230, http://dx.doi.org/10.1103/PhysRevB.41.1227, https://link.aps.org/doi/10.1103/PhysRevB.41.1227.

[77] For ONCV-QE, we employ Perdew-Burke-Ernzerhof (PBE) [66] norm-conserving pseudopotentials generated by the code ONCVPSP (Optimized Norm-Conserving Vanderbilt PSeudopotential) [75], which are downloaded from the PseudoDojo [86].

[78] The RRKJ pseudopotentials are generated by using the Opium code with the input files provided by the developers [87].

[79] K. Nakamura, S. Sakai, R. Arita, K. Kuroki, Phys. Rev. B 88 (2013) 125128, http://dx.doi.org/10.1103/PhysRevB.88.125128, https://link.aps.org/doi/10.1103/PhysRevB.88.125128.

[80] GPL Web page [online, cited https://www.gnu.org/].

[81] xTAPP Web page [online, cited http://xtapp.cp.is.s.u-tokyo.ac.jp].

[82] mVMC Web page [online, cited https://issp-center-dev.github.io/mVMC/docs/index.html].

[83] HΦ Web page [online, cited http://issp-center-dev.github.io/HPhi/index.html].

[84] A.A. Mostofi, J.R. Yates, Y.-S. Lee, I. Souza, D. Vanderbilt, N. Marzari, Comput. Phys. Comm. 178 (9) (2008) 685–699, http://dx.doi.org/10.1016/j.cpc.2007.11.016, http://www.sciencedirect.com/science/article/pii/S0010465507004936.

[85] M. Kawamura, Comput. Phys. Comm. 239 (2019) 197–203, http://dx.doi.org/10.1016/j.cpc.2019.01.017, http://www.sciencedirect.com/science/article/pii/S0010465519300347.

[86] M. van Setten, M. Giantomassi, E. Bousquet, M. Verstraete, D. Hamann, X. Gonze, G.-M. Rignanese, Comput. Phys. Comm. 226 (2018) 39–54, http://dx.doi.org/10.1016/j.cpc.2018.01.012, http://www.sciencedirect.com/science/article/pii/S0010465518300250.

[87] RRKJ pseudopotential Web page [online, cited https://www.sas.upenn.edu/rappegroup/research/pseudo-potential-gga.html].